Cell Reports

Article

Distinct fibroblast assemblies establish scarless regeneration

Graphical abstract

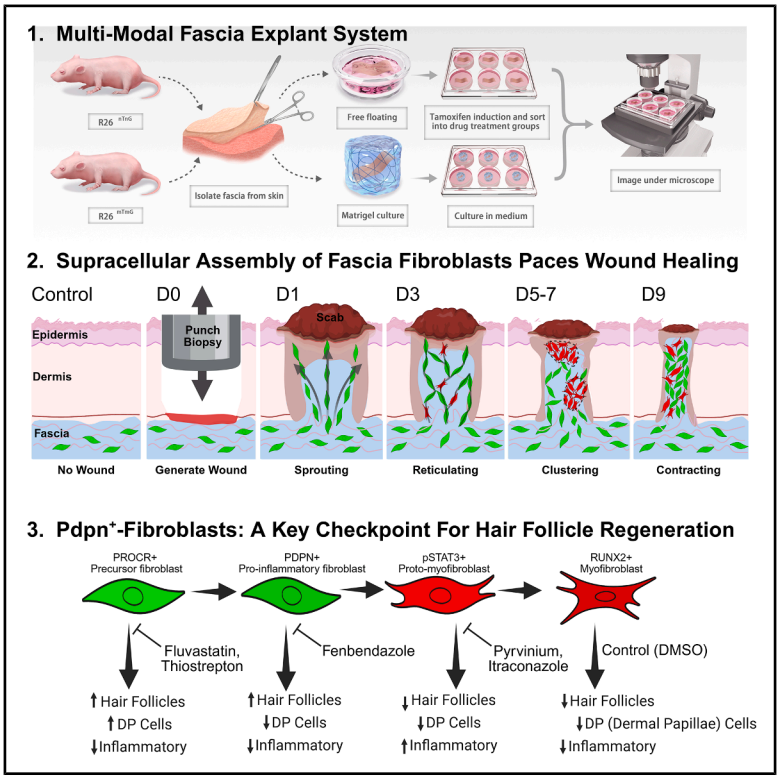

Highlights

- Fascia fibroblasts coordinate as supracellular assemblies during healing
- Fibroblast organization patterns predict wound recovery better than matrix deposition
- Three drugs block fibroblast sprouting and enable scar-free regeneration
- Drug screen reveals spectrum from fibrotic to regenerative wound healing

Authors

Haifeng Ye, Qing Yu, Alvin John Kim Seong Lee, ..., Kamyar Hadian, Hans-Günther Machens, Yuval Rinkevich

Correspondence

yuval.rinkevich@cimrbj.ac.cn

In brief

This study reveals that wound fibroblasts organize into supracellular assemblies that sprout, reticulate, and cluster, with these patterns predicting healing outcomes better than traditional markers. Drugs that block early sprouting prevent scarring and promote regenerative healing with hair follicle regrowth, offering new therapeutic approaches for wound healing and fibrotic disorders.

Ye et al., 2026, Cell Reports *45*, 116767
January 27, 2026
https://doi.org/10.1016/j.celrep.2025.116767

CellPress

Cell Reports

CellPress
OPEN ACCESS

Article

Distinct fibroblast assemblies establish scarless regeneration

Haifeng Ye,[1,11] Qing Yu,[2,11] Alvin John Kim Seong Lee,[3,11] Wendan Dong,[3,11] Zhenyu Chang,[3] Donovan Correa-Gallegos,[4] Dongsheng Jiang,[5,6] Ruoxuan Dai,[7] Kenji Schorpp,[8] Kamyar Hadian,[8] Hans-Günther Machens,[9] and Yuval Rinkevich[3,10,12,*]

[1]Medical Center of Burn Plastic and Wound Repair, The First Affiliated Hospital, School of Basic Medical Sciences, Institute of Biomedical Innovation, Jiangxi Medical College, Nanchang University, Jiangxi, China
[2]Key Laboratory of Quantitative Synthetic Biology, Shenzhen Institute of Synthetic Biology, Shenzhen Institutes of Advanced Technology, Chinese Academy of Sciences, Shenzhen 518055, China
[3]Chinese Institutes for Medical Research, Institute of Regenerative Biology and Medicine, Beijing 100069, China
[4]Institute for Stroke and Dementia Research, Ludwig-Maximilian University, Munich, Germany
[5]Precision Research Centre for Refractory Diseases, Shanghai General Hospital, Shanghai Jiao Tong University School of Medicine, Shanghai 201620, China
[6]Trauma Medical Centre, Shanghai General Hospital, Shanghai Jiao Tong University School of Medicine, Shanghai 201620, China
[7]Department of Dermatology, Second Affiliated Hospital, Zhejiang University School of Medicine, Hangzhou, China
[8]Helmholtz Zentrum München, Assay Development and Screening Platform, Munich, Germany
[9]Technical University of Munich, School of Medicine, Klinikum rechts der Isar, Department of Plastic and Hand Surgery, Munich, Germany
[10]Capital Medical University, Beijing 100069, China
[11]These authors contributed equally
[12]Lead contact
*Correspondence: yuval.rinkevich@cimrbj.ac.cn
https://doi.org/10.1016/j.celrep.2025.116767

SUMMARY

Optimal tissue recovery requires coordinated fibroblast activity from deep fascia. Using multi-modal imaging of fascia explants from lineage-specific reporter mice, we tracked wound fibroblasts over 5 days, revealing their organization into supracellular assemblies—sprouting, reticulating, and clustering throughout healing. High-throughput screening of the Prestwick library against these fascia explants identified drugs modulating these behaviors, revealing a spectrum from fibrosis to scarless healing. Recovery phenotypes correlated with fibroblast sprouting, reticulation, and clustering rather than traditional extracellular matrix (ECM) deposition markers. We identified two therapeutic categories: compounds disrupting reticulation/clustering that inhibit scarring and compounds (fluvastatin, thiostrepton, fenbendazole) disrupting sprouting that blocked pro-inflammatory fibroblast/myofibroblast commitment, promoted angiogenesis, reduced inflammatory infiltration, and enabled scar-free regenerative healing with hair follicle papillae regrowth in mice. These findings establish fibroblast supracellular organization as fundamental to tissue recovery, providing novel therapeutic targets for wound healing and fibrotic disorders.

INTRODUCTION

Injured mammalian soft tissues and organs recover in coordinated stages that include (1) inflammation, followed by (2) scar formation, and subsequent (3) tissue contraction.[1–3] Failure to coordinate these three steps, or their persistence, can lead to healing failures, such as in chronic wounds or fibroproliferative disorders, both of which can lead to lethal organ dysfunction.[4,5] Understanding these tissue recovery mechanisms is critical, given that healing failures drive a range of conditions across multiple organ systems, including pulmonary fibrosis, systemic sclerosis, liver cirrhosis, kidney and cardiovascular disease, and macular degeneration.[6–9] While significant progress has been made in understanding skin-wound healing, fundamental questions remain regarding the coordination of cellular behaviors that distinguish optimal recovery from pathological scarring. Particularly, the role of deep-tissue fibroblasts—such as those originating from the fascia—in orchestrating tissue-scale recovery remains poorly understood. Given these knowledge gaps and their broader clinical implications, it is a matter of tremendous interest to elucidate the mechanisms underlying optimal tissue recovery.

Among the key cellular protagonists that coordinate and pace successful tissue recovery are fibroblasts.[10,11] For example, in the initial step of tissue recovery, fibroblasts regulate the timing and duration of wound inflammation.[12] These inflammatory fibroblasts release interleukins, cytokines, C–C-type chemokines, and growth factors such as platelet-derived growth factor (PDGF) and transforming growth factor β (TGF-β). These growth factors are also secreted by macrophages to further activate

fibroblasts through paracrine signaling or direct cell-cell contact.[13] In the second step, inflammatory fibroblasts differentiate into proto-myofibroblasts, followed by a third and final step where contractile fibroblasts, termed myofibroblasts,[14] mechanically transform the wound bed by contracting on wound-inundated matrixes that originates from adjacent fascia[15] and *de novo* collagen synthesis. This feedforward loop of matrix deposition and contraction leads to newly rebuilt scar tissue that exhibits a shortened tissue, with isotropic, dense, and stiffened fiber organization and reduced porosity.[16–18] These biomechanical and structural constraints hinder optimal tissue recovery and regeneration.[19] Current treatment options under clinical development do not aim for optimal tissue recovery and regeneration but rather reduce collagen synthesis through TGF-β and integrin signaling and thus reduce forces between fibroblasts and the extracellular matrix (ECM).[20,21] Although *de novo* collagen synthesis is an important facet of tissue recovery, the key to optimal recovery without excessive tissue inflammation, scarring, and contraction is how wound fibroblasts self-organize and coordinate.[22,23]

Fascia are sheets of connective tissues underneath the skin that span the entire body.[24] Human fascia is divided into four layers—superficial fascia (subcutaneous), deep fascia, visceral fascia, and parietal fascia. Fascial thickness directly affects scar formation; areas such as the chest, back, and upper arms have thicker fascia and are prone to forming hypertrophic scars and keloids. Oral mucosa and genital skin lack subcutaneous fascia and form minimal scars. Female fascia is 15% thicker than male fascia, but female skin is 55% thinner and are more prone to pathological scarring.[25] Mouse fascia is located between the *panniculus carnosus* and skeletal muscle, achieving wound closure through fascial contraction, while human fascia is positioned above the skeletal muscle, interspersed within adipose tissue, extending upward to connect with the dermis. It serves as a depot of fibroblast precursors "on standby" for injury response, from which they are shunted into sites of injury to plug wounds.[15,26] Recently, we identified a multipotent fibroblast progenitor in the fascia that differentiates during the healing process of wounded skin.[27] Fascia mobilization occurs through three stages of differentiation: fibroblast precursors commit toward expressing the stem and progenitor cell surface marker for the protein kinase C receptor (Procr),[28,29] then differentiate into pro-inflammatory fibroblasts marked by Podoplanin (Pdpn), and then into proto-myofibroblasts marked by signal transducer and activator of transcription 3 (Stat3), which finally differentiates to myofibroblasts marked by Runt-Related Transcription Factor 2 (Runx2).[27] The identification of these markers provided new avenues for studying fibroblastic lineage commitment during tissue recovery.

In mice, deep wounds, i.e., injuries that traverse through the *panniculus carnosus* muscle and superficial fascia layers (equivalent to depths seen in third-degree thermal injuries) succumb to severe scars.[30] Humans lack a *panniculus carnosus*.[31] Here, the process of scarring—especially pathological scarring—is triggered once the deep dermal layer has been destroyed (e.g., by injury or in people with an inborn tendency to develop keloids).[32] In children or in people of color, the occurrence such of hypertrophic scars or keloids are more likely to have detrimental effects on both their physical appearance and psychological well-being. If the fascial layer underneath the subcutaneous tissue is damaged, scarring can occur at the wound-bed site.[30] However, complete loss or destruction of the fascia layer due to severe burns or lacerations or trauma that leaves the underlaying tissue (nerves, blood vessels, muscles, tendons, and bones) unprotected leads to severe fibrotic scars that never resolve and are often accompanied by chronic pain and reduced functionality. One treatment option for wounds of such critical depths requires harvesting functionally and aesthetically adequate tissue from other parts of the body then surgically transplanting it onto the affected site. In summary, the fascial layer is a biologically mandatory matrix for tissue recovery in mouse models and in humans. Without fascial tissue, the risk of infection and loss of deeper tissue structures is significantly increased.

Despite advances in understanding wound healing, the mechanisms underlying optimal recovery from deep wounds remain incompletely understood. We hypothesized that fibroblasts originating from the deep fascia coordinate their behavior at the tissue level to orchestrate optimal wound recovery and that disruption of this coordination may distinguish pathological scarring from regenerative healing. To test this hypothesis, we developed a multi-modal fascia explant system using gel cultures of fascia, fascial explants suspended in medium, skin-intact fascial explants, and finally *in vivo* models using injured animals. While the suspended fascia explant assay allowed us to intuitively observe contraction of fascia tissue, the Matrigel-embedded 3D model of fascia explants better mimicked the *in vivo* environment, which permitted extended live imaging to explore the dynamic remodeling of fascia fibroblasts at the single cellular level, including their sprouting, reticulation, and clustering events. Using fascia fibroblast lineage-specific reporter mice, we employed live imaging to capture the dynamic cellular behaviors that occur during tissue recovery. We then integrated this system with high-throughput drug screening to systematically perturb fibroblast coordination and identify cellular behaviors that are critical for optimal healing outcomes. Finally, we validated our findings using *in vivo* wound-healing mouse models to determine whether manipulation of these cellular behaviors could improve healing outcomes in living animals. This approach allows us to bridge single-cell behaviors with tissue-scale recovery and identify new therapeutic targets for wound healing and fibrotic disorders.

RESULTS

Fibroblast supracellular dynamics coordinate their phenotypes and functions

Current studies of *in vivo* fibroblastic healing responses are limited by the depth into the body that cells can be visualized and by the extended multi-day processes of wound healing. This limits the ability to view the complete dynamics of fibroblasts from precursors onwards in their native connective tissue environments in deep wounds.

To study fibroblast precursors enacting contraction and scarring of deep wounds, we developed a multi-modal fascia explant system using free-floating and gel-based cultures to separately image fibroblasts in their native fascia connective tissue and in fascia explants taken from multiple fascia fibroblast reporter mouse lines (Figures 1A and 1B). This multi-modal system

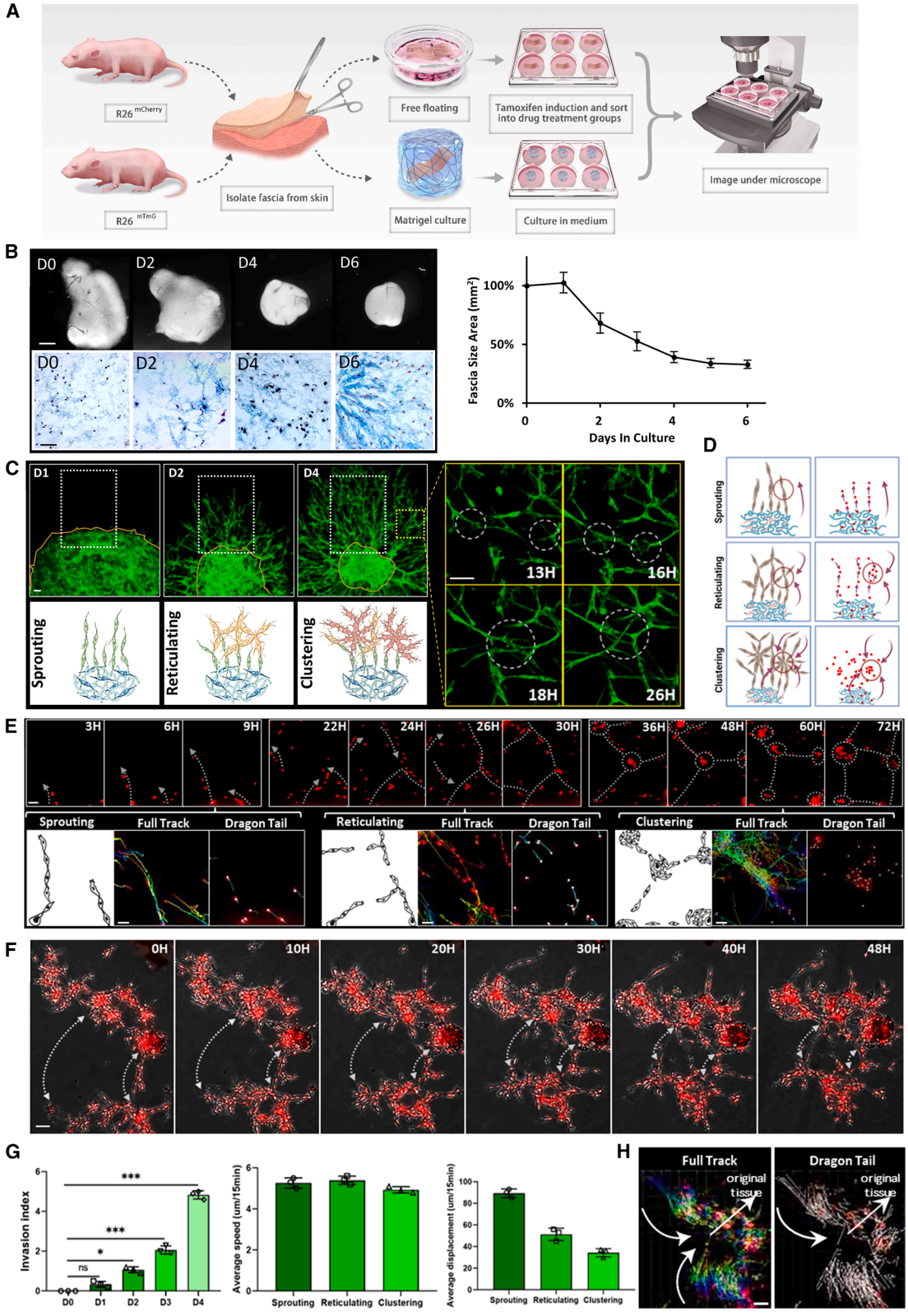

(legend on next page)

enables us to offset potential mechanical artifacts that are inherent to a cell culture system by preserving the cells in the native tissue, thus maintaining the physically relevant microenvironment, the interactions with other cell types, and the tissue structure to maximally mimic the *in vivo* environment. To image fibroblast precursors, we combined our multi-modal systems with mouse lines that could report on the presence of fascia fibroblasts,[33] removing adventitial and perivascular fibroblast observations and immune cells from our single-cell imaging. We crossed fibroblastic lineage reporter mice (*En1*^{Cre}) with transgenic reporter mice (*R26*^{mTmG}) to generate double-transgenic offspring (*En1*^{Cre};*R26*^{mTmG}) expressing membrane-bound green fluorescence protein (GFP) from the *En1* promoter, thereby genetically tagging En1-lineage-positive fibroblasts (EPFs) in the fascia. Using high-resolution fluorescence imaging with two-photon excitation (Figure S1A) and a fixed, stable incubation chamber for multi-modal fascia explants, we videoed communities of fascia EPFs in their native connective tissue perpetually over 5 days (Figure S1B).

Using the Matrigel-based system, we observed fascia EPFs displaying supracellular connectivity with increasing convolutions over time (Figure 1C), first sprouting or migrating in multicellular convoys, then interconnecting with nearby sprouts to form web-like reticulation patterns and gradually congregating into cell clusters (Figure 1D). Video S1 shows a 3D view of the interconnecting cellular web formed by fascia EPFs. Video S2 shows these interconnecting cellular reticula within the fascia jelly (snapshots in Figure 1C). To further analyze fibroblast cooperations, we opted for a system that labels fascia EPF nuclei instead of cell membranes (Figure 1E). For this, we crossed *En1*^{Cre} mice to a nuclear mCherry reporter line (*R26*^{mCherry}). This cross enables viewing fibroblast cooperations more clearly and allows computational tracking and mapping of single cells in living tissues over days. Long-term videoing and recording of live fascia from these mice over 5 days reveal stereotypic sprouting, reticulations, and clustering, validating these three principal assemblies of fibroblasts at the supracellular level (Video S3; snapshots in Figure 1E). All three assemblies were temporally and spatially sequenced. Sprouting occurs first and initiates proximal to the core fascia tissue, generating multicellular radial protrusions within 1–2 days post-injury that serves as convolution anchor points. Reticulations between fibroblastic sprouts commences from day 2 and occurs only in staggered fibroblasts located in distal locations. The third phase, fibroblast aggregation and clustering, emerges at 3 to 5 days post injury (DPI) and occurs only in the distal margins away from the injured tissue. As reticulation networks become increasingly convoluted, cell/nuclear density increases over time to form dense contractile cellular clusters. Video S4 records two clusters of fascia fibroblasts from the free-floating model merging over time to form a single interconnecting cluster, forming new reticulation networks and undergoing further contraction (snapshots in Figure 1F). These observations show fascia EPFs acting in a cooperative fashion during the three assembly phases and not individually. Importantly, these dynamics are absent from dermal (Video S5) and oral-cavity (Video S6) fibroblasts.

Next, we use automatic single-cell tracking to analyze fibroblast cell displacements during sprouting, reticulation, and clustering assemblies (Figure 1G). This sequence enables the detection of coordinated cell displacements of single cells, from 92 μm down to 54 μm and to 34 μm, across the three assembly phases. This reflects fascia fibroblasts undergoing high migratory displacement during the sprouting phase, moderate displacement as they form reticulating networks with neighboring fibroblast sprouts, and low displacement during the clustering phase. Velocity analysis of single cells across the three assembly phases indicates that fibroblasts also coordinate migration velocity at speeds of 5.5, 5.7, and 4.9 μm/15 min/track, respectively. Overall, these data show a dynamic spatiotemporal coordination of EPFs across the three assembly phases (Figure 1H).

Fibroblast supracellular dynamics coordinate their differentiation

During tissue recovery, fibroblast proliferation is paced after inflammation.[34] Consistent with this, whole-tissue 3D immuno-labeling across the three assembly phases indicate that cellular

Figure 1. Characterizing sprout, reticulate, and cluster assemblies of fascia fibroblasts

(A) Schematic diagram of the multi-modal fascia explant system developed to image fibroblasts from native fascia and fascia explants taken from *En1*^{Cre};*R26*^{mTmG} and *En1*^{Cre};*R26*^{mCherry} reporter mouse lines.

(B) Left: dynamic changes in suspended fascia cultures from day 0 to day 6 (D0–D6) under stereomicroscopy and histological processing. Right: quantification of fascia contraction under stereomicroscopy ($n > 5$; data are represented as mean ± SEM).

(C) Top left: representative images of fascia fibroblasts from *En1*^{Cre};*R26*^{mTmG} mice embedded in Matrigel undergoing sprouting (D1), reticulating (D2), and clustering (D4) assemblies using two-photon microscopy; fascia explants are outlined in green. Bottom left: cartoon schematics representing events in white-dotted frames. Right: high-resolution representative images of fibroblasts forming interconnecting networks outside the fascia over time, represented using green-dotted frames; "H" denotes time in hours.

(D) Schematic representation of fascia fibroblasts undergoing sprout, reticulate, and cluster assemblies; left column represents observations from *En1*^{Cre};*R26*^{mTmG} fibroblasts (C); right column represents observations from *En1*^{Cre};*R26*^{mCherry} nuclei (E).

(E) Top: computational tracking and mapping of fascia embedded in Matrigel showing nuclei from *En1*^{Cre};*R26*^{mCherry} mice undergoing sprouting (3–9 h), reticulating (22–30 h) and clustering (36–72 h) assemblies; white-dotted lines and circles denote migration and cluster events. Bottom: schematic diagram, full-track and dragon-tail tracking of each assembly.

(F) Snapshots of two suspended fascia cultures demonstrating clusters of fibroblasts merging over time; white-dotted lines indicate fixed points from both clusters.

(G) Analysis of live-imaging fibroblast tracks (E) migrating out of the fascia "invasion index" from D0–D4 and fibroblast migration velocity ("average speed") and displacement ("average displacement"); frames 1–49 for sprouting; frames 52–125 for reticulating; frames 126–299 for clustering ($n = 3$, data are represented as mean ± SEM).

(H) Coordination of fibroblasts in suspended fascia cultures across the three assembly phases in response to wounding.

Scale bars: 1 mm (B), 50 μm (C, E, F, and H).

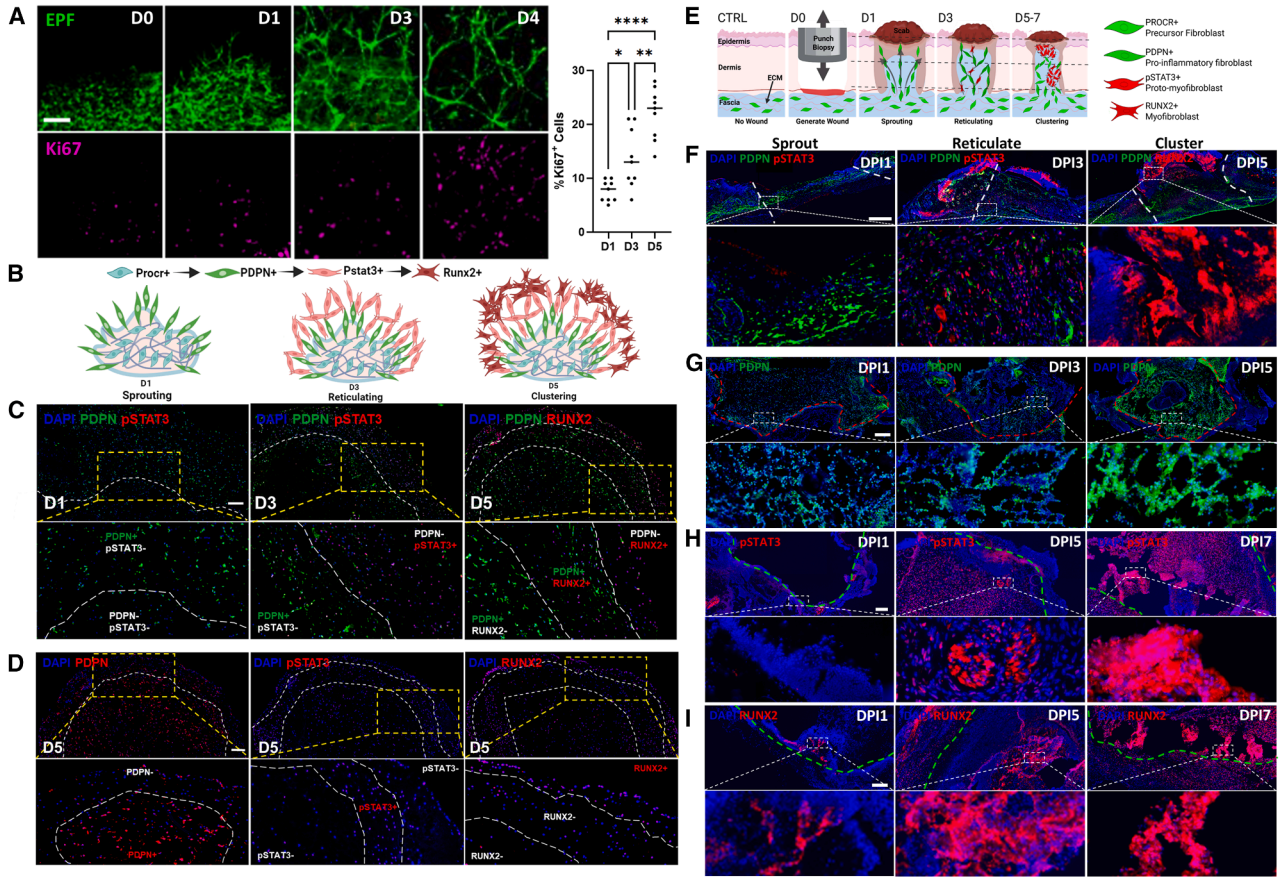

Figure 2. Spatiotemporal distributions of fibroblast lineages during sprout, reticulate, and cluster assemblies

(A) Left: Ki67 immunolabelling of Matrigel-cultured En1-lineage-positive fibroblasts (EPFs) from *En1*^{Cre};*R26*^{mTmG} mice over D0–D5. Right: scatterplot quantification.

(B) Schematic representation of the spatiotemporal distributions of fascia fibroblast lineages.

(C and D) Representative confocal microscopy images demonstrating the spatiotemporal distributions of suspended fascia culture fibroblast lineages (Procr^{+} precursor fibroblasts, Pdpn^{+} pro-inflammatory fibroblasts, pStat3^{+} proto-myofibroblasts, Runx2^{+} myofibroblasts) during D1–D5; white-dotted lines separate the inner-outer regions of the fascia; yellow-dotted frames represent the regions where high-resolution representative images were obtained.

(E) Schematic representation outlining the spatiotemporal distribution of fibroblast lineages after wounding.

(F–I) Representative confocal microscopy image panel demonstrating *in vivo* spatiotemporal distributions of fibroblast lineages from lateral (F) and transverse (G–I) tissue sections from deep wounds undergoing sprout assembly at 1 day post-injury (DPI1), reticulate assembly between 3 and 5 days post-injury (DPI3–5), and cluster assembly between 5 and 7 days post-injury (DPI5–7); each panel consists of one low-resolution image of the wound and adjacent non-wounded area, and one high-resolution image represented by dotted frames in the low-resolution image; white- (F) or green-dotted (G–I) lines in the low-resolution images demarcate wound and unwounded regions; white-dotted (F) lines in the high-resolution images demarcate deep and shallow regions of the lateral tissue section. Scale bars: 50 μm (A), 100 μm (C and D), and 250 μm (F–I).

proliferation is paced in the fascia after sprouting and peaks during the reticulation and clustering assembly phases (Figure 2A). Video S7 records EPFs proliferating during migration (snapshots in Figure S1C). Taken together with our previous results using 2D (Figure S1D) and 3D culture (Figures 1C and 1E) and cell clearance data that show no tissue contraction when fascia fibroblasts were removed (Figure S1E), we propose fascia fibroblasts are responsible for coordinating migration speeds and velocity, migration trajectories, and cell divisions by organizing into the sprout-reticulate-cluster assemblies (Figure 2B).

After characterizing EPFs undergoing the three assembly phases and their proposed involvement in wound healing, we turned toward investigating the spatial and temporal distributions of the four fascia fibroblast lineage differentiation stages (Procr^{+} precursors, Pdpn^{+} pro-inflammatory, pStat3^{+} proto-myofibroblasts, Runx2^{+} myofibroblasts) during the sprout-reticulate-cluster phases (Figures 2C and S2A). We confirm the expression of all four fibroblast differentiation stages—as well as end-stage phenotypical myofibroblasts (Yap^{+}, αSMA^{+})—through immunolabelling of free-floating fascia, indicating fibroblast lineage is paced during the three assemblies. More importantly, the expression of Pdpn, pStat3, and Runx2 are spatially and temporally stratified (Figure S2B). At day 1, high Pdpn expression is observed, while pStat3 and Runx2 are nearly absent. At day 3, pStat3 supplants Pdpn, indicating fibroblast lineage differentiation from pro-inflammatory toward

proto-myofibroblasts. At day 5, Runx2 in turn supplants pStat3, indicating further fibroblast lineage differentiation from proto-myofibroblasts toward myofibroblasts. Intriguingly, at day 5 there is a gradient expression of Pdpn^{high} within the fascia, pStat3^{high} adjacent to the fascia, and Runx2^{high} further outside the fascia (Figure 2D), suggesting distinct fibroblast differentiation steps are associated with different assembly phases. However, the distribution of YAP and αSMA expression is not spatially specific (Figure S2C).

To link the previously described fibroblast differentiation dynamics (Figures 2B–2D) with tissue-scale coordination (Figure S2D), we analyzed the spatial and temporal distributions of the four fascia fibroblast lineage differentiation stages *in vivo* by performing immunolabeling on lateral (Figures 2E and 2F) and transverse (Figures 2G–2I and S2E) tissue sections from deep wounds between 1 and 9 days post-injury (DPI1–9). Sprouting assemblies at DPI1 are characterized by migration of precursor fibroblasts (Procr^{+}) and their subsequent pro-inflammatory (Pdpn^{+}) progeny into the wound, with negligible involvement of proto-myofibroblasts (pStat3^{+}) or myofibroblasts (Runx2^{+}). Reticulating assemblies observed at DPI3 are characterized by increasing inter-connecting networks and higher cell densities. These assemblies also involve precursor and pro-inflammatory fibroblast progeny, as well as increasing populations of proto-myofibroblasts and myofibroblasts. Clustering assemblies from DPI5 onwards, characterized by dense cell clusters, is marked by high expression of proto-myofibroblasts and myofibroblasts. Subsequently at DPI7, while precursor and pro-inflammatory fibroblasts are present throughout in the wound region, proto-myofibroblasts and myofibroblasts appear to congregate at the edges of the wound in dense clusters. This observation of dense clusters of myofibroblasts congregating at the edges of the wound indicates its role in wound contraction, which other studies have characterized to be mediated via αSMA in cardiac tissues[35] and in skin.[36] We tested this idea using αSMA immunolabeling on transverse tissue sections (Figure S2F), which show an absence of αSMA during the sprouting (DPI1) and reticulating (DPI3) phases and present during the clustering phases (DPI5–7) and beyond (DPI9), thereby supporting the idea that myofibroblasts contribute toward wound closure following the clustering assembly. Furthermore, immunolabeling of transverse-plane tissue sections at different depths of the wound provides a novel means of visualizing the spatial-temporal organization of fascia fibroblasts compared to lateral-plane sections (Figure S2G). Collectively, these results confirm that fibroblast cell lineage differentiation is linked with supracellular assembly progression, providing a framework for coordinating tissue recovery.

Fibroblast supracellular dynamics predict scar severity and healing

Our previous data demonstrate dynamic coordination of fibroblast phenotype and function via three principal assemblies occurring in a spatiotemporal sequence. These observations are unique yet non-contradictory with other studies that investigated fibroblast heterogeneity using single-cell transcriptomes[37] or fibroblastic dynamics using collagen hydrogels, which actuate contraction through fibroblasts pulling on collagen fibers in the gels.[38] We therefore implemented our multi-modal fascia explant imaging assays with high-throughput functional screenings using the Prestwick library of 1,280 FDA-approved small molecules; paired with different experimental setups resulting in different data outputs (Figure 3A). This unbiased approach enables us to link assembly dynamics with contraction scars and identify novel and unforeseeable functions and gene ontologies that modulate fibroblast assemblies beyond intercellular adhesion.

Using full-thickness skin explants comprising dermis, hypodermis, *panniculus carnosus* muscle, and superficial fascia as the first assay, we performed two rounds of phenotypic screening of the 1,280 small molecules for non-conformity to contracture scar phenotypes and identified 26 chemicals (Table 1) that consistently change the extent of skin contraction and scar severity with a phenotypic spectrum of wound-healing outcomes (Figure 3B). To measure scar severities in high detail, we performed fractal measurements on tissues from the 26 chemicals after 5 days post-injury by determining the fractal dimensions and lacunarity values of the ECM lattice organization and combining these two values into a fractal score (Figure 3C). Fractal dimensions quantify how completely a fractal fills a space at increasing levels of magnification, which indicates the complexity level of an object. The lacunarity value reflects the porosity and heterogeneity of an object. Thus, severe scars have high fractal dimensions and lower lacunarity values than normal uninjured skin, and wounds with delayed healing have the reverse tendency.

Based on the overall histomorphology (Figure 3B) and fractal score (Figure 3C), we categorize these 26 chemicals into four distinct phenotypic subgroups. Subgroup "non-healing wound" is characterized by high lacunarity and low fractal dimension and includes seven chemicals that are predicted to delay wound healing with thin and loosely linked reticular matrix. Subgroup "normal skin," characterized by lacunarity and fractal dimension values similar to unwounded (normal) skin and wounds from oral tissue, includes six chemicals that are predicted to promote scarless wound healing. Subgroup "scar," characterized by lacunarity and fractal dimension values similar to scarred skin and wounds treated with DMSO, includes six chemicals that are predicted to promote normal skin scarring with a normally dense and cross-linked matrix. Subgroup "severe scar," characterized by low lacunarity and high fractal dimension, includes seven chemicals that were predicted to promote severe scars extending beyond the skin explant borders with abnormally dense matrix and fibroblast foci. To be noted, the first two subgroups of compounds dramatically reduced scarring with non-existent skin contraction (1% "hit" rate). These chemically treated skin explants remain flat and resemble chronic wounds even after 5 days in culture. Among the normal skin subtype of chemicals that confer scar values close to normal skin are itraconazole "1139," pyrvinium pamoate "1040," thiostrepton "522," and fluvastatin sodium "859." These compounds' therapeutic classes include anti-fungal, anti-bacterial, anti-tumor, anti-helminthic, and anti-lipemic compounds with diverse modes of action (Table 1). As they may be conferring anti-scarring properties by modifying supracellular organization and fibroblast differentiation at distinct steps, we designated these drugs as

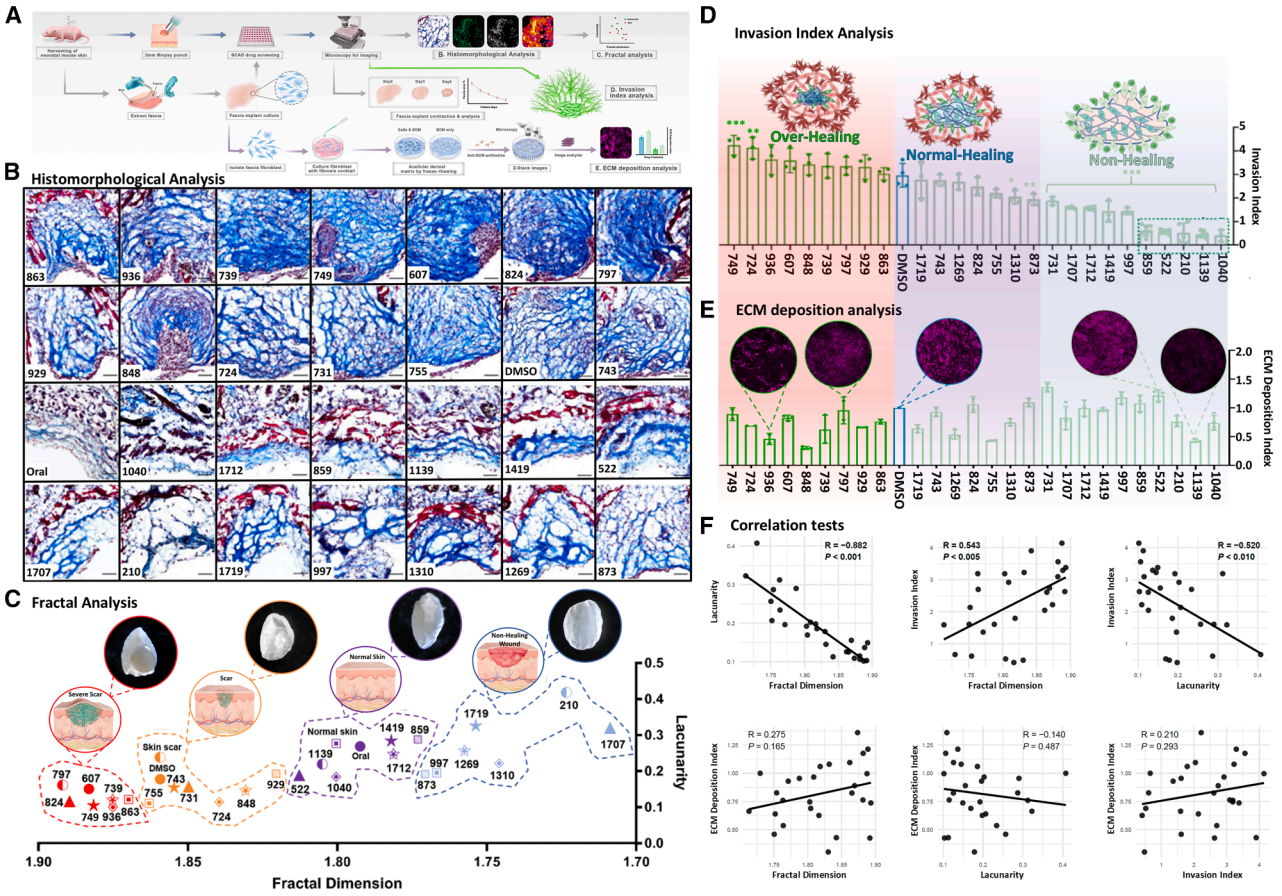

Figure 3. Implementing multi-modal fascia explant imaging assays with high-throughput functional screenings

(A) Schematic diagram outlining the implementation of multi-modal fascia explant imaging assays with high-throughput functional screenings to generate a range of experimental data types.

(B) Representative histology images of whole-skin explants after treatment with chemicals, 26 of which showed aberrant scarring effect (anti- or pro-scarring) with a clear trend on scarring severity; DMSO serves as control; oral serves as an additional control.

(C) Fractal dimension and lacunarity analysis of histomorphological analysis (B). Histomorphological analysis enabled the data to be divided into 4 distinct subgroups: "severe scar," "scar", "normal skin," and "non-healing wound." "Skin scar" serves as another control consisting of skin samples from wounded mice that generated a scar. Schematic diagrams made to represent four wound-healing phenotypes: "severe scar," "scar," "normal skin," and "non-healing wound." Representative stereomicroscopy images included to represent each wound-healing phenotype.

(D) Invasion index analysis of fascia fibroblasts screened with 26 chemicals and DMSO control; each treatment was compared against DMSO using one-way ANOVA; fibroblast phenotypes were re-categorized into "over-healing," "normal healing," and "non-healing" according to invasion index score; schematic diagrams included to represent each fascia fibroblast phenotype.

(E) Extracellular matrix deposition analysis of mouse primary fascia fibroblasts cultured with a fibrosis cocktail medium containing TGF-β and one of the 26 chemicals; representative 3D-reconstructed microscopy images of extracellular matrix deposition of fascia fibroblasts.

(F) Pairwise correlation analysis between supracellular dynamics (invasion index), healing phenotypes (fractal dimension, lacunarity), and extracellular matrix deposition index; tests that show both significant p values ($p < 0.05$) and R values (positive correlation, $R > 0.5$; negative correlation, $R < -0.5$) are bolded. Scale bar: 10 μm (B).

candidates for being repurposed as wound-healing agents and focused on them in subsequent experiments.

Having measured scar severities and identified potential candidates for drug repurposing, we next set out to further identify other healing phenotypes. By subjecting explants of whole skin with fascia from *En1*^{Cre};*R26*^{mTmG} mice to the 26 drugs, we measured fascia contraction (Figure S3A) and determined the fibroblast "invasion index," which measures the fibroblast's capacity for migrating out of the fascia and invading into the surrounding environment (Figures 3D and S3B). From analysis of this healing phenotype, we sorted the chemicals into three groups: "over-healing," which we predict leads to excessive scarring; "non-healing," which we predict results in open wounds that fails to close; and "normal healing," which we predict is a balance of the two extremes. Interestingly, the four chemicals (itraconazole "1139," pyrvinium pamoate "1040," thiostrepton "522," and fluvastatin sodium "859") that previously conferred scar values close to normal skin (Figure 3C) and inhibited fascia contraction ($p < 0.001$) (Figure S3A) impede supracellular assembly with a reduced rate of migration speed and migration velocity

Table 1. Hit summary from drug library screening

No.	Chemicals	Therapeutic class	Therapeutic effects	Mode of action	SCAD effect[a]
1040	pyrvinium pamoate	metabolism	anti-helminthic	casein kinase 1a activator	– – – –
1712	flumethasone pivalate	dermatology	anti-inflammatory	glucocorticoid receptor agonist	– – –
859	fluvastatin sodium	cardiovascular	anti-lipemic	HMG-CoA reductase inhibitor	– – – –
522	thiostrepton	infectiology	anti-bacterial; anti-tumor	FOXM1 inhibitor	– – – –
1139	itraconazole	infectiology	anti-fungal; anti-tumor	cytochrome P450 enzymes inhibitor	– – – –
1419	fluocinolone acetonide	endocrinology	anti-inflammatory	glucocorticoid receptor agonist	– – – –
1707	doxapram hydrochloride	respiratory	analeptic	potassium channel inhibitor	– – –
1719	amorolfine hydrochloride	infectiology	anti-fungal	D-14-reductase and D-7,8-isomerase inhibitor	– – –
210	fenbendazole	infectiology	anti-helminthic	tubulin blocker	– – –
997	fluticasone propionate	cardiovascular	anti-inflammatory	glucocorticoid receptor agonist	– –
1310	phenylbutazone	metabolism	anti-inflammatory	prostaglandin G/H synthase 2 inhibitor	– –
1269	haloprogin	infectiology	anti-fungal	possibly inhibits oxygen update, disrupts membrane	– –
873	theophylline monohydrate	respiratory system	bronchodilator	adenosine receptor (antagonist)	–
724	sulfamethoxypyridazine	infectiology	anti-bacterial	dihydropteroate synthase inhibitor	–
929	ketorolac tromethamine	CNS	analgesic	prostaglandin G/H synthase 2 inhibitor	–
731	sulfaquinoxaline sodium	infectiology	anti-bacterial	vitamin K epoxidase inhibitor	–
755	piperacillin sodium	infectiology	anti-bacterial	penicillin-binding proteins inhibitor	+
743	medrysone	metabolism	anti-inflammatory	glucocorticoid receptor agonist	+
749	isoetharine mesylate	respiratory	bronchodilator	adrenergic beta-2 agonist	+
863	etidronate disodium	metabolism	anti-osteoporosis	ATP inhibitor	+
936	bephenium hydroxynaphthoate	metabolism	anti-helminthic	B-type AChR activator	+
848	iodixanol	diagnostic	contrast	X-ray contrast activity	+
607	eburnamonine (–)	CNS	vasodilator	muscarinic acetylcholine receptor M1–M4 modulator	+ + +
739	levonordefrin	cardiovascular	vasoconstrictor	adrenergic receptor alpha-2 agonist	+ +
797	levomepromazine maleate	CNS	analgesic	adrenergic receptor and dopamine receptor antagonist	+ + +
824	benzthiazide	cardiovascular	anti-hypertensive	inhibit Na^+/Cl^- reabsorption in kidneys	+ + +

[a]"–" represents decreased scarring; "+" represents increased scarring; more symbols represent stronger effect.

compared to DMSO control (Figures S3C and S3D), and overall displayed the lowest invasive index (Figure 3D). Indeed, these four chemicals were ranked having the fifth-, fourth-, second-, and first-lowest invasion index, respectively. Interestingly, the chemical with the third-lowest invasion index was fenbendazole "210," also an anti-helminthic (Table 1), albeit conferring scar values among the non-healing subtype of chemicals (Figure 3C). Due to its low invasion index ($p < 0.001$) and impeding supracellular assembly properties (Figures S3B–S3D), we decided to include it among our drug candidates for further experiments. Meanwhile, many chemicals in the severe scar subtype (Figure 3C) displayed the highest invasion index (Figure 3D), indicating a correlation between fibroblast hyperactivity and excessive scarring due to wound over-healing.

To determine if *de novo* ECM deposition could be an alternative healing phenotype predictor, we performed a deposition assay with the 26 drugs using primary fascia fibroblasts isolated from mice and cultured under a fibrosis cocktail medium containing TGF-β to induce *de novo* deposition (see STAR Methods) (Figure 3E). Control primary cultures received fibrosis cocktail alone, whereas 78 fascia cultures were supplemented with the 26 chemicals, separately, in triplicates. All fascia cultures at 7 days were subjected to fixation, and freeze-thaw cycles to remove cells, followed by immunolabeling of the acellular matrix, confocal 3D imaging for collagen type 1 and fibronectin, and fluorescence quantification of each well for deposited matrix. Analysis of the ECM deposition shows none of the trends observed with fractal analysis or invasion index, indicating no correlation between fibroblast ECM deposition and wound-healing phenotypes. To validate the observations described among fractal analysis, invasion index analysis, and ECM deposition analysis, we examined pairwise correlations between supracellular dynamics and healing phenotypes across different drug treatment conditions (Figure 3F). Notably, no significant

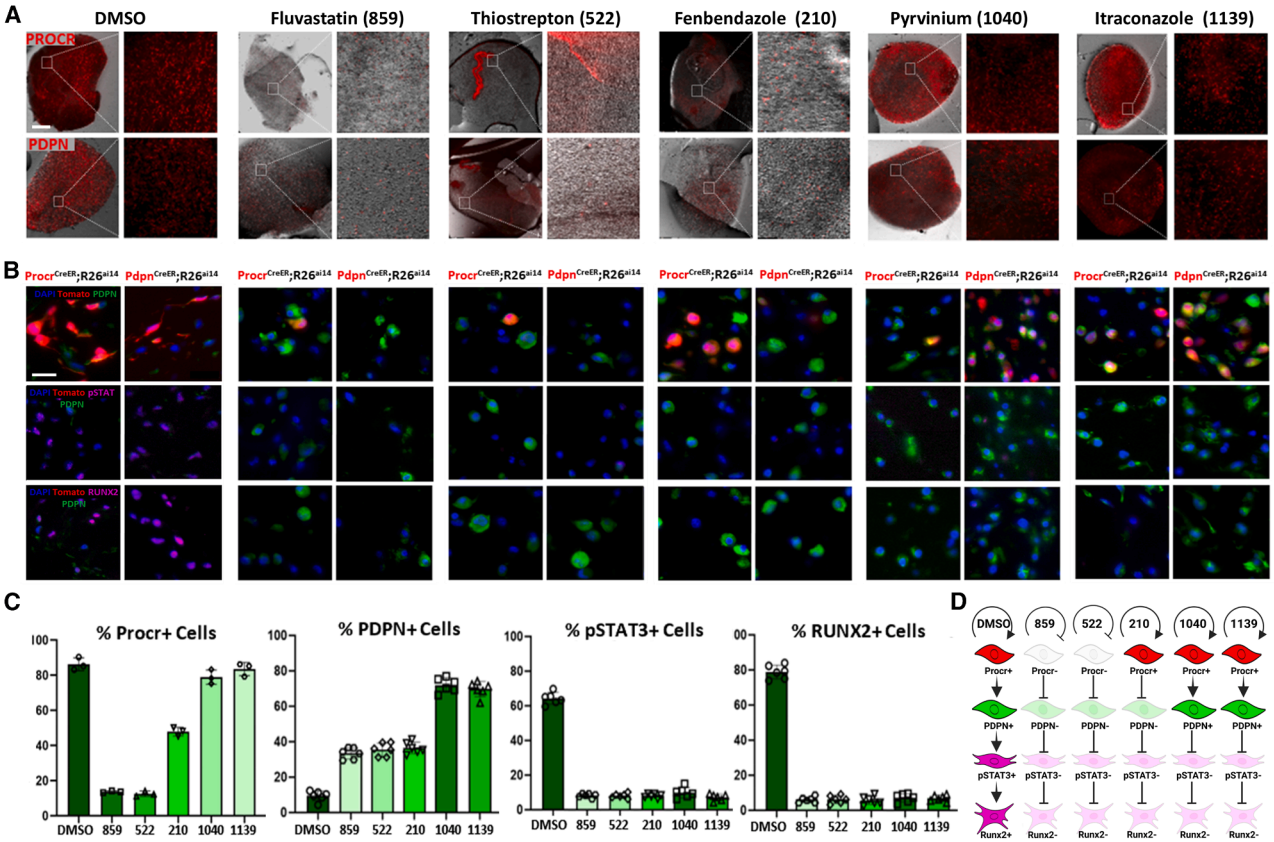

Figure 4. Fascia fibroblast lineage commitment is stalled at distinct steps

(A) Panel of representative low- and high-resolution images of suspended fascia culture explants from *Procr*^{CreER};*R26*^{ai14} (top row) and *Pdpn*^{CreER};*R26*^{ai14} mice (bottom row), cultured in the candidate chemicals for repurposing (fluvastatin sodium "859"; thiostrepton "522"; fenbendazole "210"; pyrvinium pamoate "1040"; itraconazole "1139") or control (DMSO); white-dotted frames represent regions where high-resolution images were obtained; fibroblast precursors (Procr^{+}) and inflammatory commitment-state fibroblasts (Pdpn^{+}) tagged with TomatoRed.

(B and C) High-resolution microscopy image panel (B) and quantification (C) demonstrating that *Procr*^{CreER};*R26*^{ai14} (left column) and *Pdpn*^{CreER};*R26*^{ai14} (right column) fascia fibroblast lineage commitment are stalled at distinct stages by the chemicals in suspended fascia cultures ($n \geq 3$; data are represented as mean ± SEM).

(D) Schematic diagram of fascia fibroblast lineage commitment being stalled at distinct steps after chemical culture.

Scale bars: 1 mm (A), 25 μm (B).

correlation was observed between ECM deposition index and fractal dimension or lacunarity or invasion index, while invasion index exhibited significant correlations with both fractal dimension and lacunarity ($p < 0.05$). Correlation between fractal dimension and ECM deposition index was significant only in the five chemicals (itraconazole "1139," pyrvinium pamoate "1040," thiostrepton "522," fenbendazole "210," and fluvastatin sodium "859") that reduced scar values ($p < 0.05$) (Figure S3E). These results indicate that collagen type 1 and fibronectin deposition in 2D cultures do not predict wound outcomes.

Two distinct assembly steps lead to scarless healing

Having identified candidate drugs for repurposing that confer anti-scarring properties and are correlated with supracellular modulation, we next examined which steps of fibroblast lineage commitment are stalled. To directly identify the commitment stage being modulated by these drugs, we combined *Procr*^{CreER};*R26*^{ai14} and *Pdpn*^{CreER};*R26*^{ai14} genetic lineage tracing with immunolabeling of fibroblast stage specific commitment markers. Live fascia tissues isolated from *Procr*^{CreER};*R26*^{ai14} mice contain fascia fibroblast precursors (Procr^{+}), and fascia tissues isolated from *Pdpn*^{CreER};*R26*^{ai14} contain fibroblasts at the inflammatory commitment state (Pdpn^{+}), both of which are tagged with TomatoRed (Figure 4A). Fascia explants from *Procr*^{CreER};*R26*^{ai14} and from *Pdpn*^{CreER};*R26*^{ai14} double transgenic mice ($n \geq 3$) were inhibited at the fascia fibroblast precursor stage when treated with fluvastatin "859" (14.2% Procr^{+}, 34.7% Pdpn^{+}, 8.7% pStat3^{+}, 6.3% Runx2) and thiostrepton "522" (11.3% Procr^{+}, 36.2% Pdpn^{+}, 8.2% pStat3^{+}, 6.2% Runx2). Treatment with fenbendazole "210" (50.6% Procr^{+}, 35.6% Pdpn^{+}, 8.6% pStat3^{+}, 6.4% Runx2) results in fascia fibroblasts being unable to exit the precursor state (Procr^{high}) into the pro-inflammatory state. To confirm these results are not affected by other factors such as proliferation or apoptosis, we performed Ki67 and caspase-3 immunolabelling and found both events to be low and unaffected by chemical treatment (Figure S3F).

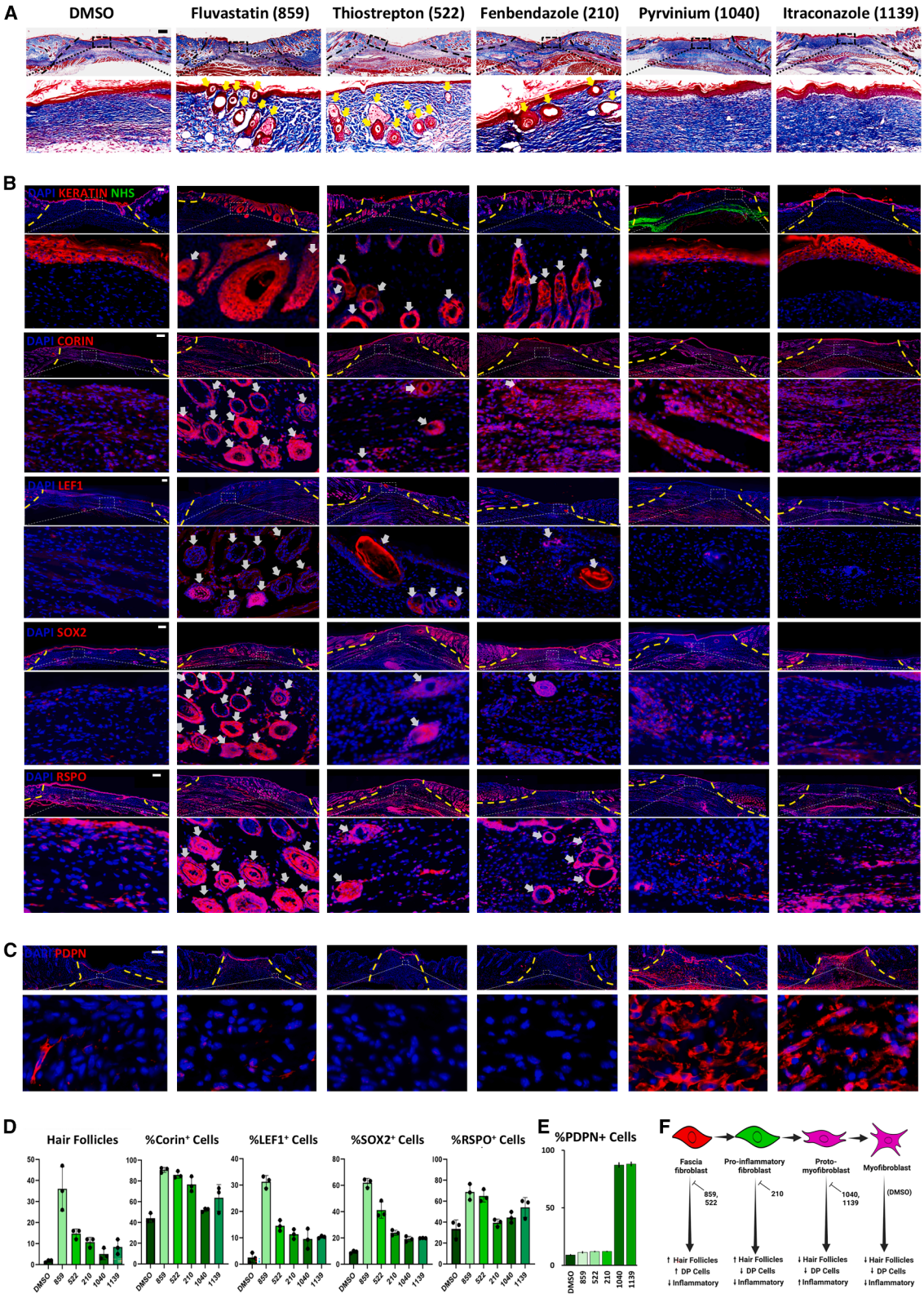

(legend on next page)

Finally, treatment with pyrvinium "1040" (74.5% Procr^{+}, 70.5% Pdpn^{+}, 8.5% pStat3^{+}, 7.5% Runx2) and itraconazole "1139" (81.3% Procr^{+}, 69.3% Pdpn^{+}, 8.3% pStat3^{+}, 7.3% Runx2) results in fibroblasts persisting in the pro-inflammatory state (Pdpn^{high}) and unable to transition into the proto-myofibroblast (pStat3^{high}) commitment states. Lastly, all chemically treated explants fail to differentiate into Runx2^{+} myofibroblasts (Figures 4B and 4C). Other papers have also separately shown itraconazole and pyrvinium pamoate to inhibit myofibroblast differentiation.[39,40] However, our genetic lineage tracing combined with chemical treatments indicate that pyrvinium and itraconazole block myofibroblast differentiation while perpetuating PDPN^{+} pro-inflammatory fibroblast states, whereas the other three anti-scar chemicals (fluvastatin, thiostrepton, fenbendazole) did not (Figure 4D). Overall, these results indicate that myofibroblast blockade at an advanced post-inflammatory commitment stage may be detrimental to wound healing, whereas blocking before the inflammatory commitment step may be optimal for wound healing.

Modulation of early precursor commitment unlocks tissue recovery with regeneration

Having found these anti-scarring chemicals blocking fibroblast cooperations and differentiations at distinct steps, we next sought to test their effects on wound healing *in vivo* (Figure S4A). Briefly, 6 mm full thickness wounds were generated on mouse back skin using punch biopsies, allocated to different treatment groups, and treated with chemicals every other day by subcutaneous injection (see STAR Methods). Interestingly, treating mice with the candidate drugs results in slightly decreased rates of wound closure up till day 9 before contracting faster afterward (Figure S4B). Consistent with our previously described *in vitro* observations, immunofluorescence staining of *in vivo* wounds show that all five chemicals block myofibroblast (Runx2) differentiation (Figure S5A) and block N-cadherin expression (Figure S5B), indicating these drugs blocking cell-cell connections in myofibroblasts.

At advanced recovery day 21, a remarkable skin-regeneration phenotype emerges in these *de novo* wounds (total mice $n = 48$; $n = 8$ per chemical treatment group)—hair-follicle regrowth (Figure 5A). Newly formed hair follicles emerged throughout the wound area after treatment with fluvastatin (38 ± 8 follicles), with clearly visible hair shafts growing in most of the newly formed follicles marked by abundant expression of keratin and high numbers of dermal papillae cells (average 11,100 Corin^{+}, 3,615 Lef1^{+}, 8,957 Sox2^{+}, 7,952 Rspo2^{+}) within the newly forming hair follicles and within the connective tissue bellow the hair shafts (Figures 5B and 5D). Wounds treated with thiostrepton (11 ± 5 follicles) and fenbendazole (14 ± 7 follicles) also demonstrate hair-follicle regeneration with accompanying keratin expression but fewer dermal papillae cells (average 5,151 and 3,465 Corin^{+}, 502 and 394 Lef1^{+}, 3,998 and 1,190 Sox2^{+}, 3,439 and 2,424 Rspo2^{+}). Finally, hair-follicle regeneration is absent or negligible in wounds treated with pyrvinium (3 ± 1 follicles) and itraconazole (4 ± 1 follicles), marked by low keratin and low numbers of dermal papillae cells (average 3,072 and 4,123 Corin^{+}, 529 and 576 Lef1^{+}, 1,276 and 1,396 Sox2^{+}, 2,652 and 3,649 Rspo2^{+}); all similar to control wounds treated with DMSO (2 ± 1 follicles). In addition, wounds treated with itraconazole and pyrvinium resulted in enhanced PDPN^{+} pro-inflammatory fibroblasts (Figures 5C and 5E), consistent with our *in vitro* observations (Figure 4C).

Besides hair-follicle regeneration, we also explored other key processes of wound healing such as angiogenesis (vascular endothelial cells, CD31) and immune cell (inflammatory macrophage, CD80; neutrophil, Ly6G) infiltration. Within the wound region, we observed a mild increase of vascular marker CD31 following fluvastatin, thiostrepton, and fenbendazole treatment and reduction following pyrvinium and itraconazole treatment (Figure S5C). These data indicate that chemical treatment also affects immune cell infiltration into the wound region. Inflammatory macrophage infiltration is blocked by fluvastatin, thiostrepton, and fenbendazole, while enhanced by pyrvinium and itraconazole (Figure S5D). And interestingly, all five chemicals cause increased neutrophil infiltration (Figure S5E). Finally, we utilized a localized N-cadherin knockout model (see STAR Methods) to determine whether disruption of cell-cell adhesion affects fascia fibroblast differentiation. Using this model, we collected DPI14 wounds and stain them for PDPN or pStat3 or Runx2. We observed enhanced PDPN^{+} but reduced pStat3^{+} or Runx2^{+} cells in the N-cadherin knockout group (Figure S5F). These data support the previously described reduction of N-cadherin^{+} cells following chemical treatment (Figure S5B) and overall indicate that these chemicals may be blocking Runx2^{+} myofibroblast differentiation through disruption of cell-cell adhesion.

Overall, our results indicate that modulation of assembly at the Procr^{+} precursor stage with repurposed fluvastatin—and to a lesser extent fenbendazole or thiostrepton—unlocks skin regeneration by promoting dermal papillae cell expression and *de novo* hair follicle regrowth (Figure 5F). These

Figure 5. Modulation of early precursor fibroblasts unlocks hair-follicle regeneration *in vivo*

(A) Panel of representative low- (top row) and high-resolution (bottom row) Masson's trichrome images of wounds 27 days after injury, demonstrating hair-follicle regeneration within the wound region of mice treated with fluvastatin "859," thiostrepton "522," and fenbendazole "210"; black dotted lines demarcate wound and unwounded regions; black dotted frames represent regions where high-resolution images were taken.

(B) Panel of representative low- and high-resolution confocal microscopy images, demonstrating enhanced cytokeratin (keratin) and derma papilla cells (Corin, Lef1, Sox2, RSPO) within the wound region of mice treated with fluvastatin, thiostrepton, and fenbendazole; yellow dotted lines demarcate wound and unwounded regions; white dotted frames represent regions where high-resolution images were taken.

(C) Panel of representative low- (top row) and high-resolution (bottom row) confocal microscopy images, demonstrating enhanced inflammatory commitment-state fibroblasts (Pdpn^{+}) when mice were treated with pyrvinium "1040" and itraconazole "1139"; yellow dotted lines demarcate wound and unwounded regions; white dotted frames represent regions where high-resolution images were taken.

(D and E) Graphical representation of the quantitative analysis of (A)–(C), ($n = 3$; data are represented as mean ± SEM).

(F) Schematic diagram outlining inhibition of fascia fibroblast lineage unlocks hair-follicle regeneration.

Scale bars: 250 μm (A–C).

regeneration phenotypes repeatedly emerge in experiments where early precursor commitment is blocked and where contracture scar formation is suppressed in wounds. Our animal experiments and multi-modal fascia explant models indicate that hair-follicle regeneration only emerges during an early temporal window, when the early precursor excess to PDPN^{+} cells is blocked, accompanied by an increase in the vascular marker CD31 and a decrease in macrophages. However, blockade of fibroblasts at the later assembly step results in augmentation of pro-inflammatory (Pdpn^{+}) fibroblasts, with a decrease in the vascular marker CD31 and an increase in macrophages, marked by absence of hair-follicle regeneration and low numbers of derma papillae cells. Ultimately, our results indicate that readout of fibroblast supracellular assembly are predictive of tissue recovery and provide a new context for therapeutic intervention.

DISCUSSION

Fibroblast supracellular assemblies mediate differentiation and regeneration

Here, we uncover an elegant system whereby fascia fibroblasts coordinate their differentiation, activation, proliferation, and migration, which facilitates successful wound healing with *de novo* hair-follicle regeneration. At the heart of this coordination mechanism are increased cell convolutions in three stages by three stereotypic supracellular assemblies of sprouting, reticulations, and clustering (Figure 1 and S1). These assemblies are spatial-temporally organized during wound healing (Figures 2 and S2), and variations in this supracellular organization could affect timely and successful tissue recovery. We hypothesize that several factors may influence the efficacy of this supracellular coordination system. First, we propose that the fibroblast cell states (whether metabolic, senescent, apoptotic, proliferative) within these supracellular frames could affect the system's ability to dynamically respond. We further hypothesize that successful tissue recovery may also depend on density and size of the supracellular clusters that sprout upon injury. Additionally, we propose that the clinical implications of supracellular assemblies may depend also on the strength of connections between adjacent reticulated and clustered cells, potentially mediated by molecules such as N-cadherin or Connexin gap junctions.[33,41] We suggest that these supracellular structures may allow fibroblasts to monitor and perceive biophysical or signaling information and translate or propagate the cues across the tissue for organized responses.

A recent publication suggests that blocking mechanotransduction in EPFs with the Yap/Taz mechanotransduction signaling inhibitor Verteporfin, induces a scar-free regenerative healing in mice.[42] Our data suggest that in a scenario of deep wounds, blocking mechanotransduction along with myofibroblast commitment is not enough, whereas blocking the early passage of fibroblast precursors before pro-inflammatory commitment elicits a dual effect of reducing mechanotransduction and inflammation and elicits a regenerative scenario in deep wounds. We confirm regeneration outputs with three separate drugs that span across a range of therapeutic classes (Table 1), validating fibroblast supracellular assemblies as reliable predictors for scar severity and healing outcomes (Figures 3 and S3).

The relationship between fascia-derived fibroblasts and hair follicles is unclear and a subject of ongoing research.[43,44] In mice, hair-follicle regrowth is not observed in small (<1 cm diameter) excisional wound models. However, in larger wounds models (>1 cm diameter) hair-follicle regeneration can be observed during the remodeling phase, approximately after 14 days after injury.[45,46] In this study, which utilizes the 5 mm biopsy punch wound model, we observed changes in fascia fibroblast lineages *in vitro* following drug treatment (Figure 4) and a decrease in *in vivo* wound closure rate up till 9 days after injury (Figure S4). These results imply that blocking fascia fibroblasts from entering the proto- (pStat3) and myofibroblast (Runx2) stages are conducive to wound healing. Lastly, we observed pronounced hair-follicle regeneration and enhanced dermal papilla cells *in vivo* when wounded mice were treated with fluvastatin, thiostrepton, and fenbendazole (Figure 5), along with suppressed myofibroblast (Runx2), dysregulation of cell-cell adhesion (N-cad), and increased immune cell infiltration (Figure S5). The reduction of N-cadherin is of particular interest, as disruption of N-cadherin in cancer-associated fibroblasts are associated with increased migratory and invasive characteristics.[41] Taken together, our data indicate fluvastatin, thiostrepton, and fenbendazole playing a novel role in wound healing with renewed hair-follicle regeneration by suppressing late-stage myofibroblast differentiation and maintaining a pro-migratory environment. That said, other key processes in wound healing—consequences of immune cell infiltration, involvement of other fibroblasts, angiogenesis, re-epithelialization—were not covered in the scope in this study. Future work should explore these processes to better characterize these chemicals' functional roles in wound-healing.

Potential mechanisms of fluvastatin, thiostrepton, and fenbendazole in hair-follicle regeneration

Fluvastatin belongs to the statin class of drugs, which inhibits high-mobility group (HMG)-coenzyme A (CoA) reductase in the mevalonate pathway to reduce cholesterol synthesis.[47] Several pathways suggest fluvastatin may promote hair-follicle regeneration. First, fluvastatin's inhibition of the RhoA/ROCK pathway could facilitate hair follicle stem cell activation, as RhoA/ROCK signaling is known to maintain stem cell quiescence in the hair-follicle bulge.[48] Second, fluvastatin's enhancement of bone formation through the BMP-2/Smad pathway[31] may be relevant to hair-follicle morphogenesis, where BMP signaling regulates follicle cycling and dermal papilla cell function.[32] Third, the anti-inflammatory properties of fluvastatin targeting *p*-AKT/mTOR signaling and the NLRP3 inflammasome[33] could create a permissive microenvironment for hair-follicle regeneration by reducing chronic inflammation that typically inhibits follicular recovery.

Thiostrepton's inhibition of FOXM1 may promote hair-follicle regeneration through distinct mechanisms other than its anti-cancer effects.[49] FOXM1 regulates cell cycle progression, and its modulation could influence the coordinated proliferation required during anagen initiation in hair-follicle cycling. Additionally, thiostrepton's effects on antioxidant proteins such as

Peroxiredoxin3 may protect hair-follicle stem cells and dermal papilla cells from oxidative stress that can impair regenerative capacity.[50]

Fenbendazole's microtubule-targeting mechanism and activation of the AMPK/mTOR pathway suggest potential roles in hair-follicle regeneration.[51–53] Microtubule dynamics are crucial for the directional cell movements during hair-follicle morphogenesis, while AMPK signaling regulates cellular energy homeostasis in rapidly proliferating hair matrix cells during anagen.

Overall, our results suggest that these three drugs create a favorable environment for skin regeneration by blocking the early precursor transition to PDPN$^+$ cells, increasing angiogenesis and reducing the number of inflammatory cells in the wound environment, and ultimately promote hair-follicle regeneration. Finally, we propose that outputs of supracellular assembly could be broadly applicable for drug-repurposing strategies across wound healing and fibrotic diseases.

Conclusion

Dynamic supracellular assemblies coordinate fibroblast lineage differentiations, activations, and migrations to pace tissue recovery. Moreover, supracellular dynamics is predictive of tissue-recovery phenotypes. Using supracellular dynamics as output, a bipolar phenotype emerges with anti-scarring drugs, with the specific outcome depending on where fibroblast differentiation is stalled. Here, the sprouting phase—marked by a Pdpn$^+$ pro-inflammatory state—represents a key checkpoint for optimal tissue recovery by regeneration. Fluvastatin, thiostrepton, and fenbendazole act on this checkpoint by restricting fibroblast differentiation, disrupting cell-cell adhesion, increasing angiogenesis, and reducing inflammatory macrophage infiltration, overall generating an ideal microenvironment conducive for new hair-follicle regeneration within wounds. Our findings reveal fibroblast supracellular organization as a fundamental feature of optimal tissue recovery and provide a new context for therapeutic interventions across a range of wound-healing and fibrotic disorders.

Limitations of this study

In this study, we combined multiple *in vivo* and *in vitro* models and a high-throughput chemical library screening to identify chemicals that inhibited scar formation and overall promoted regeneration. However, these studies were all carried out in mouse, and the experiments of chemical performance in treating human samples are lacking. The effects of these chemicals on human wound healing recovery need further investigation. Besides, we illustrated that these scar-inhibiting chemicals work through prevention of one of the four fascia fibroblast lineage differentiation stages (Procr$^+$ precursors, Pdpn$^+$ pro-inflammatory, pStat3$^+$ proto-myofibroblasts, and Runx2$^+$ myofibroblasts). Whether this differentiation and scar-inhibition mechanism is the same in human fascia fibroblasts during wound healing is not clear.

RESOURCE AVAILABILITY

Lead contact

Requests for further information and resources should be directed to and will be fulfilled by the lead contact, Yuval Rinkevich (yuval.rinkevich@cimrbj.ac.cn).

Materials availability

This study did not generate new, unique reagents.

Data and code availability

- All data reported in this paper will be shared by the lead contact upon request.
- This paper does not report original code.
- Any additional information required to re-analyze the data reported in this paper is available from the lead contact upon request.

ACKNOWLEDGMENTS

Y.R. is supported by funds from the Chinese Institutes for Medical Research. H.Y. was supported by the China Scholarship Council, National Natural Science Foundation of China (82572888, 82402919), and the Jiangxi Province Natural Science Foundation (20252BAC200109). Q.Y. was supported by the China Scholarship Council. D.C.-G. was supported by the Consejo Nacional de Ciencia y Tecnología (CONACYT) and the Deutscher Akademischer Austauschdienst (DAAD).

AUTHOR CONTRIBUTIONS

Y.R. outlined the research and wrote the manuscript. Q.Y. performed the 3D tissue culture, 3D staining and imaging, cell tracking, and data analysis. Q.Y., D.J., and K.S. performed the primary screening. H.Y. performed the 3D tissue culture and fascia floating culture and performed the immunofluorescence staining, image editing, and data analysis. A.J.K.S.L. collected data and structured the paper. W.D. performed and analyzed all animal experiments. Q.Y. and D.C.-G. performed live imaging. Z.C. provided technical support for skeleton analysis. R.D. assisted with data analysis.

DECLARATION OF INTERESTS

The authors have submitted a patent application related to medicals for hair-follicle regeneration.

STAR★METHODS

Detailed methods are provided in the online version of this paper and include the following:

- KEY RESOURCES TABLE
- EXPERIMENTAL MODEL AND STUDY PARTICIPANT DETAILS
  - Mouse lines & animal experiments
  - Localized N-cadherin knockout in *R26*^{Cas9} mouse
- METHOD DETAILS
  - Full thickness skin explants model
  - Fascia explants in matrigel model
  - Fascia suspension cultures model
  - Prestwick chemical library (PCL) & high throughput screening
  - Splinted wound model
  - Decellularized fascia preparation
  - Migration & contraction measurements
  - Histology
  - *In vivo* chemical treatment to unlock regeneration
  - Whole mount tissue staining & imaging
  - Live imaging
  - Single-cell tracking
  - ECM deposition and immunostaining assay
- QUANTIFICATION & STATISTICAL ANALYSIS
  - Data analysis
  - Statistics & reproducibility

SUPPLEMENTAL INFORMATION

Supplemental information can be found online at https://doi.org/10.1016/j.celrep.2025.116767.

Received: June 12, 2025
Revised: November 18, 2025
Accepted: November 27, 2025

REFERENCES

1. Henderson, N.C., Rieder, F., and Wynn, T.A. (2020). Fibrosis: from mechanisms to medicines. Nature *587*, 555–566. https://doi.org/10.1038/S41586-020-2938-9.
2. Ho, Y.Y., Lagares, D., Tager, A.M., and Kapoor, M. (2014). Fibrosis - A lethal component of systemic sclerosis. Nat. Rev. Rheumatol. *10*, 390–402. https://doi.org/10.1038/NRRHEUM.2014.53.
3. Distler, J.H.W., Györfi, A.H., Ramanujam, M., Whitfield, M.L., Königshoff, M., and Lafyatis, R. (2019). Shared and distinct mechanisms of fibrosis. Nat. Rev. Rheumatol. *15*, 705–730. https://doi.org/10.1038/S41584-019-0322-7.
4. Eming, S.A., Martin, P., and Tomic-Canic, M. (2014). Wound repair and regeneration: Mechanisms, signaling, and translation. Sci. Transl. Med. *6*, 265sr6. https://doi.org/10.1126/SCITRANSLMED.3009337.
5. Ezzo, M., Spindler, K., Wang, J.B., Lee, D., Pecoraro, G., Cowen, J., Pakshir, P., and Hinz, B. (2024). Acute contact with profibrotic macrophages mechanically activates fibroblasts via αvβ3 integrin-mediated engagement of Piezo1. Sci. Adv. *10*, eadp4726. https://doi.org/10.1126/SCIADV.ADP4726.
6. Buckley, C.D., Rainger, G.E., Bradfield, P.F., Nash, G.B., and Simmons, D.L. (1998). Cell adhesion: More than just glue (review). Mol. Membr. Biol. *15*, 167–176. https://doi.org/10.3109/09687689709044318.
7. Wei, K., Korsunsky, I., Marshall, J.L., Gao, A., Watts, G.F.M., Major, T., Croft, A.P., Watts, J., Blazar, P.E., Lange, J.K., et al. (2020). Notch signalling drives synovial fibroblast identity and arthritis pathology. Nature *582*, 259–264. https://doi.org/10.1038/S41586-020-2222-Z.
8. Mizoguchi, F., Slowikowski, K., Wei, K., Marshall, J.L., Rao, D.A., Chang, S.K., Nguyen, H.N., Noss, E.H., Turner, J.D., Earp, B.E., et al. (2018). Functionally distinct disease-associated fibroblast subsets in rheumatoid arthritis. Nat. Commun. *9*, 789. https://doi.org/10.1038/S41467-018-02892-Y.
9. Bruera, S., Chavula, T., Madan, R., and Agarwal, S.K. (2022). Targeting type I interferons in systemic lupus erythematous. Front. Pharmacol. *13*, 1046687. https://doi.org/10.3389/FPHAR.2022.1046687.
10. Phan, Q.M., Sinha, S., Biernaskie, J., and Driskell, R.R. (2021). Single-cell transcriptomic analysis of small and large wounds reveals the distinct spatial organization of regenerative fibroblasts. Exp. Dermatol. *30*, 92–101. https://doi.org/10.1111/EXD.14244.
11. Phan, Q.M., Fine, G.M., Salz, L., Herrera, G.G., Wildman, B., Driskell, I.M., and Driskell, R.R. (2020). Lef1 expression in fibroblasts maintains developmental potential in adult skin to regenerate wounds. eLife *9*, e60066. https://doi.org/10.7554/ELIFE.60066.
12. Landén, N.X., Li, D., and Ståhle, M. (2016). Transition from inflammation to proliferation: a critical step during wound healing. preprint at Birkhauser Verlag AG *73*, 3861–3885. https://doi.org/10.1007/s00018-016-2268-0.
13. Buechler, M.B., Fu, W., and Turley, S.J. (2021). Fibroblast-macrophage reciprocal interactions in health, fibrosis, and cancer. Immunity *54*, 903–915. https://doi.org/10.1016/J.IMMUNI.2021.04.021/ASSET/71DAEF58-C3BF-44D5-99B1-945B1958009A/MAIN.ASSETS/GR3_LRG.JPG.
14. Younesi, F.S., Miller, A.E., Barker, T.H., Rossi, F.M.V., and Hinz, B. (2024). Fibroblast and myofibroblast activation in normal tissue repair and fibrosis. Nat. Rev. Mol. Cell Biol. *25*, 617–638. https://doi.org/10.1038/S41580-024-00716-0.
15. Correa-Gallegos, D., Jiang, D., Christ, S., Ramesh, P., Ye, H., Wannemacher, J., Kalgudde Gopal, S., Yu, Q., Aichler, M., Walch, A., et al. (2019). Patch repair of deep wounds by mobilized fascia. Nature *576*, 287–292. https://doi.org/10.1038/S41586-019-1794-Y.
16. Xue, M., and Jackson, C.J. (2015). Extracellular Matrix Reorganization During Wound Healing and Its Impact on Abnormal Scarring. Adv. Wound Care *4*, 119–136. https://doi.org/10.1089/WOUND.2013.0485.
17. Darby I.A., Desmoulière A. Scar Formation: Cellular Mechanisms. Textbook on Scar Management 2020;Chapter 3:19–26. doi:10.1007/978-3-030-44766-3_3.
18. Ud-Din, S., and Bayat, A. (2022). Classification of Distinct Endotypes in Human Skin Scarring: S.C.A.R.—A Novel Perspective on Dermal Fibrosis. Adv. Wound Care *11*, 109–120. https://doi.org/10.1089/WOUND.2020.1364.
19. Li, Y.Y., Ji, S.F., Fu, X.B., Jiang, Y.F., and Sun, X.Y. (2024). Biomaterial-based mechanical regulation facilitates scarless wound healing with functional skin appendage regeneration. Mil. Med. Res. *11*, 13. https://doi.org/10.1186/S40779-024-00519-6.
20. Akhurst, R.J., and Hata, A. (2012). Targeting the TGFβ signalling pathway in disease. Nat. Rev. Drug Discov. *11*, 790–811. https://doi.org/10.1038/NRD3810.
21. Györfi, A.H., Matei, A.E., and Distler, J.H.W. (2018). Targeting TGF-β signaling for the treatment of fibrosis. Matrix Biol. *68–69*, 8–27. https://doi.org/10.1016/j.matbio.2017.12.016.
22. Hamanaka, R.B., and Mutlu, G.M. (2021). The role of metabolic reprogramming and de novo amino acid synthesis in collagen protein production by myofibroblasts: Implications for organ fibrosis and cancer. Amino Acids *53*, 1851–1862. https://doi.org/10.1007/S00726-021-02996-8.
23. Wilkinson, H.N., and Hardman, M.J. (2020). Wound healing: cellular mechanisms and pathological outcomes. Open Biol. *10*, 200223. https://doi.org/10.1098/RSOB.200223.
24. Langevin, H.M. (2021). Fascia mobility, proprioception, and myofascial pain. Life *11*, 668. https://doi.org/10.3390/LIFE11070668.
25. Correa-Gallegos, D., and Rinkevich, Y. (2022). Cutting into wound repair. FEBS J. *289*, 5034–5048. https://doi.org/10.1111/FEBS.16078.
26. Wan, Y., Wei, Z., Looger, L.L., Koyama, M., Druckmann, S., and Keller, P.J. (2019). Single-Cell Reconstruction of Emerging Population Activity in an Entire Developing Circuit. Cell *179*, 355–372.e23. https://doi.org/10.1016/j.cell.2019.08.039.
27. Correa-Gallegos, D., Ye, H., Dasgupta, B., Sardogan, A., Kadri, S., Kandi, R., Dai, R., Lin, Y., Kopplin, R., Shenai, D.S., et al. (2023). CD201^{+} fascia progenitors choreograph injury repair. Nature *623*, 792–802. https://doi.org/10.1038/S41586-023-06725-X.
28. Wang, D., Cai, C., Dong, X., Yu, Q.C., Zhang, X.O., Yang, L., and Zeng, Y.A. (2015). Identification of multipotent mammary stemcells by protein C receptor expression. Nature *517*, 81–84. https://doi.org/10.1038/NATURE13851.
29. Liu, C., Lin, C., Wang, D., Wang, J., Tao, Y., Li, Y., Chen, X., Bai, L., Jia, Y., Chen, J., and Zeng, Y.A. (2022). Procr functions as a signaling receptor and is essential for the maintenance and self-renewal of mammary stem cells. Cell Rep. *38*, 110548. https://doi.org/10.1016/j.celrep.2022.110548.
30. Lin, X., and Lai, Y. (2024). Scarring Skin: Mechanisms and Therapies. Int. J. Mol. Sci. *25*, 1458. https://doi.org/10.3390/IJMS25031458.
31. Naldaiz-Gastesi, N., Bahri, O.A., López de Munain, A., McCullagh, K.J.A., and Izeta, A. (2018). The panniculus carnosus muscle: an evolutionary enigma at the intersection of distinct research fields. J. Anat. *233*, 275–288. https://doi.org/10.1111/JOA.12840.
32. Rippa, A.L., Kalabusheva, E.P., and Vorotelyak, E.A. (2019). Regeneration of Dermis: Scarring and Cells Involved. Cells *8*, 607. https://doi.org/10.3390/CELLS8060607.
33. Jiang, D., Christ, S., Correa-Gallegos, D., Ramesh, P., Kalgudde Gopal, S., Wannemacher, J., Mayr, C.H., Lupperger, V., Yu, Q., Ye, H., et al. (2020). Injury triggers fascia fibroblast collective cell migration to drive scar formation through N-cadherin. Nat. Commun. *11*, 5653. https://doi.org/10.1038/S41467-020-19425-1.
34. Willenborg, S., Lucas, T., Van Loo, G., Knipper, J.A., Krieg, T., Haase, I., Brachvogel, B., Hammerschmidt, M., Nagy, A., Ferrara, N., et al. (2012).

CCR2 recruits an inflammatory macrophage subpopulation critical for angiogenesis in tissue repair. Blood *120*, 613–625. https://doi.org/10.1182/BLOOD-2012-01-403386.

35. Shinde, A.V., Humeres, C., and Frangogiannis, N.G. (2017). The role of α-smooth muscle actin in fibroblast-mediated matrix contraction and remodeling. Biochim. Biophys. Acta. Mol. Basis Dis. *1863*, 298–309. https://doi.org/10.1016/J.BBADIS.2016.11.006.
36. McAndrews, K.M., Miyake, T., Ehsanipour, E.A., Kelly, P.J., Becker, L.M., McGrail, D.J., Sugimoto, H., LeBleu, V.S., Ge, Y., and Kalluri, R. (2022). Dermal αSMA$^+$ myofibroblasts orchestrate skin wound repair via β1 integrin and independent of type I collagen production. EMBO J. *41*, e109470. https://doi.org/10.15252/EMBJ.2021109470.
37. Xie, T., Wang, Y., Deng, N., Huang, G., Taghavifar, F., Geng, Y., Liu, N., Kulur, V., Yao, C., Chen, P., et al. (2018). Single-Cell Deconvolution of Fibroblast Heterogeneity in Mouse Pulmonary Fibrosis. Cell Rep. *22*, 3625–3640. https://doi.org/10.1016/j.celrep.2018.03.010.
38. Brunel, L.G., Long, C.M., Christakopoulos, F., Cai, B., Johansson, P.K., Singhal, D., Enejder, A., Myung, D., and Heilshorn, S.C. (2025). Interpenetrating networks of fibrillar and amorphous collagen promote cell spreading and hydrogel stability. Acta Biomater. *193*, 128–142. https://doi.org/10.1016/J.ACTBIO.2025.01.009.
39. Bollong, M.J., Yang, B., Vergani, N., Beyer, B.A., Chin, E.N., Zambaldo, C., Wang, D., Chatterjee, A.K., Lairson, L.L., and Schultz, P.G. (2017). Small molecule-mediated inhibition of myofibroblast transdifferentiation for the treatment of fibrosis. Proc. Natl. Acad. Sci. USA *114*, 4679–4684. https://doi.org/10.1073/PNAS.1702750114.
40. Jeon, K.I., Phipps, R.P., Sime, P.J., and Huxlin, K.R. (2017). Antifibrotic Actions of Peroxisome Proliferator-Activated Receptor γ Ligands in Corneal Fibroblasts Are Mediated by β-Catenin–Regulated Pathways. Am. J. Pathol. *187*, 1660–1669. https://doi.org/10.1016/j.ajpath.2017.04.002.
41. Nguyen, T., and Mège, R.M. (2016). N-Cadherin and Fibroblast Growth Factor Receptors crosstalk in the control of developmental and cancer cell migrations. Eur. J. Cell Biol. *95*, 415–426. https://doi.org/10.1016/J.EJCB.2016.05.002.
42. Mascharak, S., des Jardins-Park, H.E., Davitt, M.F., Griffin, M., Borrelli, M.R., Moore, A.L., Chen, K., Duoto, B., Chinta, M., Foster, D.S., et al. (2021). Preventing Engrailed-1 activation in fibroblasts yields wound regeneration without scarring. Science *372*, eaba2374. https://doi.org/10.1126/SCIENCE.ABA2374.
43. Ji, S., Zhu, Z., Sun, X., and Fu, X. (2021). Functional hair-follicle regeneration: an updated review. Signal Transduct. Target. Ther. *6*, 66. https://doi.org/10.1038/s41392-020-00441-y.
44. Dekoninck, S., and Blanpain, C. (2019). Stem cell dynamics, migration and plasticity during wound healing. Nat. Cell Biol. *21*, 18–24. https://doi.org/10.1038/S41556-018-0237-6.
45. Wang, X., Hsi, T.C., Guerrero-Juarez, C.F., Pham, K., Cho, K., McCusker, C.D., Monuki, E.S., Cho, K.W.Y., Gay, D.L., and Plikus, M.V. (2015). Principles and mechanisms of regeneration in the mouse model for wound-induced hair follicle neogenesis. Regeneration (Oxf) *2*, 169–181. https://doi.org/10.1002/REG2.38.
46. Ito, M., Yang, Z., Andl, T., Cui, C., Kim, N., Millar, S.E., and Cotsarelis, G. (2007). Wnt-dependent de novo hair-follicle regeneration in adult mouse skin after wounding. Nature *447*, 316–320. https://doi.org/10.1038/NATURE05766.
47. Lawrence, J.M., and Reckless, J.P.D. (2002). Fluvastatin. Expert Opin. Pharmacother. *3*, 1631–1641. https://doi.org/10.1517/14656566.3.11.1631.
48. Yi, Z., Ke, J., Wang, Y., and Cai, K. (2020). Fluvastatin protects myocardial cells in mice with acute myocardial infarction through inhibiting RhoA/ROCK pathway. Exp. Ther. Med. *19*, 2095–2102. https://doi.org/10.3892/ETM.2020.8413.
49. Kongsema, M., Wongkhieo, S., Khongkow, M., Lam, E.W.F., Boonnoy, P., Vongsangnak, W., and Wong-Ekkabut, J. (2019). Molecular mechanism of Forkhead box M1 inhibition by thiostrepton in breast cancer cells. Oncol. Rep. *42*, 953–962. https://doi.org/10.3892/OR.2019.7225.
50. Nelson, K.J., Messier, T., Milczarek, S., Saaman, A., Beuschel, S., Gandhi, U., Heintz, N., Smalley, T.L., Lowther, W.T., and Cunniff, B. (2021). Unique Cellular and Biochemical Features of Human Mitochondrial Peroxiredoxin 3 Establish the Molecular Basis for Its Specific Reaction with Thiostrepton. Antioxidants *10*, 150. https://doi.org/10.3390/ANTIOX10020150.
51. Son, D.S., Lee, E.S., and Adunyah, S.E. (2020). The Antitumor Potentials of Benzimidazole Anthelmintics as Repurposing Drugs. Immune Netw. *20*, e29. https://doi.org/10.4110/IN.2020.20.E29.
52. Dogra, N., Kumar, A., and Mukhopadhyay, T. (2018). Fenbendazole acts as a moderate microtubule destabilizing agent and causes cancer cell death by modulating multiple cellular pathways. Sci. Rep. *8*, 11926. https://doi.org/10.1038/s41598-018-30158-6.
53. Wang, L., Xu, K., Wang, N., Ding, L., Zhao, W., Wan, R., Zhao, W., Guo, X., Pan, X., Yang, J., et al. (2022). Fenbendazole Attenuates Bleomycin-Induced Pulmonary Fibrosis in Mice via Suppression of Fibroblast-to-Myofibroblast Differentiation. Int. J. Mol. Sci. *23*, 14088. https://doi.org/10.3390/IJMS232214088.
54. Rinkevich, Y., Walmsley, G.G., Hu, M.S., Maan, Z.N., Newman, A.M., Drukker, M., Januszyk, M., Krampitz, G.W., Gurtner, G.C., Lorenz, H.P., et al. (2015). Identification and isolation of a dermal lineage with intrinsic fibrogenic potential. Science *348*, aaa2151. https://doi.org/10.1126/SCIENCE.AAA2151.
55. Tinevez, J.Y., Perry, N., Schindelin, J., Hoopes, G.M., Reynolds, G.D., Laplantine, E., Bednarek, S.Y., Shorte, S.L., and Eliceiri, K.W. (2017). TrackMate: An open and extensible platform for single-particle tracking. Methods *115*, 80–90. https://doi.org/10.1016/J.YMETH.2016.09.016.
56. "FracLac for ImageJ" https://imagej.net/ij/plugins/fraclac/FLHelp/Introduction.htm.

STAR★METHODS

KEY RESOURCES TABLE

REAGENT or RESOURCE	SOURCE	IDENTIFIER
Antibodies		
αSMA	Abcam	Cat#ab21027; RRID:AB_1951138 Cat#ab124964; RRID:AB_11129103 Cat#ab5694; RRID:AB_11212646
Caspase	Abcam	Cat#ab32499; RRID:AB_777433
Cytokeratin 14	Abcam	Cat#ab7800; RRID:AB_306091
Corin	Bioss	Cat#BS-7685R; RRID：AB_3720100
Lef1	Cell signaling	Cat#2230; RRID:AB_823558
Pdpn	Invitrogen	Cat#PDPN-112AP; RRID: AB_3720101
Pdpn	Abcam	Cat#ab10288; RRID:AB_297027
pStat3	Cell Signaling Technology	Cat#9145S; RRID: AB_3720102
Rspo2	Invitrogen	Cat#PA5-25188; RRID:AB_2542688
Runx2	Proteintech	Cat#20700-1-AP; RRID:AB_2722783
Runx2	Abcam	Cat#ab92336; RRID:AB_2049267
Sox2	Proteintech	Cat#11064-1-AP; RRID:AB_2195801
Sox2	Invitrogen	Cat#PA1-094; RRID:AB_2539862
Yap1	Proreintech	Cat#13584-1-AP; RRID:AB_2218915
Collagen I	Abcam	Cat#ab34710; RRID:AB_731684
Fibronectin	Abcam	Cat#ab23750; RRID:AB_447655
CD31	Abcam	Cat#ab222783; RRID:AB_2905525
CD80	Abcam	Cat#ab134120; RRID:AB_2928982
Ly6G	Abcam	Cat#ab25377; RRID:AB_470492
N-Cadherin	Abcam	Cat#C3865; RRID:AB_262097
Donkey anti-rabbit AF647	Life Technologies	Cat#A-31573; RRID:AB_2536183
Donkey anti-goat AF647	Life Technologies	Cat#A-21447; RRID:AB_141844
Goat anti-rabbit AF488	Abcam	Cat#ab150077; RRID:AB_2630356
Goat anti-rabbit AF594	Abcam	Cat#ab150080; RRID:AB_2313537
Bacterial and virus strains		
AAV6	Addgene #240485	Addgene_240485
AAV-Cre-GFP	Addgene #68544	Addgene_68544
AAV-gRNA-GFP	Addgene #85451	Addgene_85451
Chemicals, peptides, and recombinant proteins		
Medetomidine	MCE	Cat#HY-17034
Midazolam	MCE	Cat#HY-118645
Fentanyl	Sigma-Aldrich	Cat#F3886
Metamizole	Sigma-Aldrich	Cat#SML1488
Isoflurane	RWD	Cat#R510-22-10
Paraformaldehyde	VWR	Cat#30525-89-4
Tissue-Tek O.C.T. Compound	Sakura	Cat#4583
DMSO	Sigma-Aldrich	Cat#D8418
PEG300	Solarbio	Cat#25322-68-3
Tween-80	Biosharp	Cat#BS118-100mL
Matrigel	Corning	Cat#FALC356231
DMEM/F12	Life Technologies	Cat#10565018
FBS	Life Technologies	Cat#A3160401

(*Continued on next page*)

Continued

REAGENT or RESOURCE	SOURCE	IDENTIFIER
Non-essential amino acid	Thermo Fisher	Cat#11140035
Glutamax	Thermo Fisher	Cat# 35050061
Penicillin and streptomycin	Thermo Fisher	Cat#15140122
Glutaraldehyde	Sigma-Aldrich	Cat#340855
PBS	Thermo Fisher	Cat#10010023
4-Hydroxytamoxifen	Sigma-Aldrich	Cat#H6278-50MG
DMSO	Carl Roth	Cat#67-68-5
Gelatin	Sigma-Aldrich	Cat#48722
Triton X-100	Sigma-Aldrich	Cat#X100
Thimerosal	Sigma-Aldrich	Cat#T5125
BSA	Thermo Fisher	Cat#37525
DAPI	Invitrogen	Cat#S36939
Agarose	Biozym	Cat#840001
TGFβ1	R&D Systems	Cat#240-B-002
Sodium deoxycholate	Sigma-Aldrich	Cat#D6750-25G
Critical commercial assays		
Masson's trichrome staining kit	Sigma-Aldrich	Cat#HT15
Experimental models: Cell lines		
AAVpro 293T	Takara Bio #632273	CVCL_B0XW
FF95	Farsam et al. 2016	DOI:10.18632/oncotarget.13446
Experimental mouse models: Mouse strains		
C57BL/6J wild-type	The Jackson Laboratory	IMSR_JAX:000664
R26^{mTmG}	The Jackson Laboratory	IMSR_JAX:007576
R26^{mCherry}	The Jackson Laboratory	IMSR_JAX:023139
R26^{Cas9}	The Jackson Laboratory	IMSR_JAX:024858
En1^{cre}	The Jackson Laboratory	IMSR_JAX:007916
R26^{Ai14}	The Jackson Laboratory	IMSR_JAX:007908
Procr^{CreER}	The Jackson Laboratory	IMSR_JAX:033052
Pdpn^{CreER}	The Jackson Laboratory	IMSR_JAX:039447
Software and algorithms		
Imaris 9.3.1	Bitplane	N/A
ImageJ	Fiji	N/A

EXPERIMENTAL MODEL AND STUDY PARTICIPANT DETAILS

Mouse lines & animal experiments

C57BL/6J wild-type, R26^{Cas9}, *En1*^{Cre};*R26*^{mTmG}, *En1*^{cre};*R26*^{mCherry}, *Procr*^{CreER};*R26*^{Ai14}, *Procr*^{CreER};*R26*^{mTmG}, *Pdpn*^{CreER};*R26*^{Ai14}, *Pdpn*^{CreER};*R26*^{mTmG} were purchased from Charles River or Jackson laboratories or generated through external vendor.[54] Mice gender included male and female, aged 7–8 weeks, weight 25-30g. All animals were housed at the Capital Medical University animal facility, at constant temperature and humidity with a 12-h light cycle. Food and water were provided *ad libitum*. All animal experiments were reviewed and approved by the Capital Medical University and registered under the project AEEI-2024-276 and conducted under strict government and international guidelines. This study is compliant with all relevant ethical regulations regarding animal research. For the chemical treatment study in live mice, wounds were made in wildtype mouse back skin. Mice were anesthetized with 100μL MMF (medetomidine, midazolam and fentanyl). Dorsal hair was removed with a hair clipper, followed by hair removal cream for 3–5 min. Two full-thickness excisional wounds were created with a 5-mm diameter biopsy punch (Stiefel). A chemical solution at a final concentration of 250 μM was injected intra-dermally at a volume of 75 μL per wound immediately after wounding, and throughout 21 days post-wounding at every other day. Mice were recovered from anesthesia with an MMF antagonist and were supplied with metamizole (500 mg metamizole/250 mL drinking water) as postoperative analgesic. Scar samples were collected on D21-D35 post wounding.

Localized N-cadherin knockout in *R26*^{Cas9} mouse

We designed a guide RNA (gRNA) targeting mouse N-cadherin exon 1 using the Benchling tool. N-cadherin gRNA expressing AAV6(AAV6-NcadgRNA-GFP) was obtained by transfecting the AAVpro 293T cell line (Takara Bio 632273). Cre expressing AAV6 (AAV6-Cre-GFP) was purchased from Addgene (Addgene #6854436). 13-day-old R26^{Cas9} mice expressing Cas9 systemically were first anesthetized, and then two full-thickness excision wounds with a diameter of 2 mm were made on their backs. N-cadherin ablation was performed by daily subcutaneous injection of 20 μL of AAV6-gRNA-GFP virus (virus titer 1 × 1012/mL) in two peri wound areas. Subcutaneous injections were performed around the two wounds on day 0, 5 and 10 after wound creation. Mice were subcutaneously injected with AAV6-GFP virus without gRNA as a control. Scar samples were harvested on day 14 after injury, fixed and embedded for sectioning, followed by immunofluorescence staining, imaging, and analysis.

METHOD DETAILS

Full thickness skin explants model

Post born Day 0 (P0) neonates of C57BL/6J wild type mouse were first sacrificed by decapitation. Then dorsal back skin was isolated to make 2 mm full thickness biopsies (ø 2mm, Stiefel) that included the epidermis, dermis and deep subcutaneous fascia layers. Tissues were maintained in DMEM/F12 cell culture medium (Life Technologies) supplemented with 10% FBS (Life Technologies), 1% non-essential amino acid (Thermo Fisher), 1% Glutamax (Thermo Fisher), 1% penicillin and streptomycin (Thermo Fisher) in a 37°C incubator, supplied 5% CO_2. Medium was changed every other day until day 5 when tissues were collected and fixed for histology analysis. Note, the excised skin was submerged dermis-side up in culture media, which confined the scar-prone fibroblasts to the explant and inhibited their adherence to the tissue culture plate.

Fascia explants in matrigel model

To create a 3D environment that mimics the physiological environments *in vivo*, we established a fascia Matrigel (Corning) system. Fascia tissues were isolated by the same approach as above, but with P4 to P6 neonates of *En1*^{cre};*R26*^{mTmG} mouse lines. Cre positive neonates from this double transgenic mouse line were detected by green fluorescent signal in dorsal skin with a Leica M205 FA stereo microscope. Matrigel was prepared by diluting the stock aliquots with plain DMEM/F12 medium to a concentration of 6 mg/mL. Then 150 μL prepared gel was added in the center of a 35 mm cell culture dish (Ibidi). 4 mm biopsies were made from the dorsal skin from which the fascia tissues were then isolated. Isolated fascia tissues were then embedded into the gel and were allowed to solidify for one hour at 37°C. Then the tissue-gel system was maintained in DMEM/F12 medium supplemented with 10% FBS (both Life Technologies), 1% non-essential amino acid, 1% Glutamax, 1% penicillin and streptomycin (all Thermo Fisher) in a 37°C incubator supplied with 5% CO_2. Medium was changed every other day until day 4 when tissues were collected and fixed. For the fixation with Matrigel system, tissues were fixed in 2% paraformaldehyde (VWR) with 0.1% glutaraldehyde (Sigma) for 1 h and then washed three times with phosphate buffered saline (PBS, Life Technologies) and stored in PBS at 4°C.

Fascia suspension cultures model

The dorsal fascia of the mouse was separated, and the fascia was cut to an appropriate size. 3 mL of DMEM/F-12 complete medium was added (10% FBS, 1% NEAA, 1% penicillin and streptomycin) to a six-well plate. Between 3 and 6 fascia explants were added to each group, imaged under a microscope to monitor the dynamic changes in fascia continuously for 5–6 days, and replaced the medium every 48 h. For tamoxifen induction experiments, the overall process refers to the fascia suspension culture, the only difference is that 1 micromolar tamoxifen needs to be added at the same time on day 0, and fresh medium is replaced every 20 h. The induction of positive cells can be observed with a stereoscopic fluorescence microscope.

Prestwick chemical library (PCL) & high throughput screening

The Prestwick library contains 1280 approved (by FDA, European Medicines Agency (EMA) or other agencies) small molecules covering a range of major anatomical therapeutic classes including central nervous system (19%), cardiovascular system (11%), metabolism (24%) and infectious diseases (16%). The purity of the compounds was >90% as reported by the provider. The PCL provides an additional advantage as all chemicals are of stable physicochemical properties, show a high range of chemical diversity, and have known bioavailability and safety data in humans. All this information helps to reduce the probability of screening low-quality hits and saves the costs of preliminary screening process. In order to accommodate high throughput screening, we adapted the tissue explant system into 96-well plate (Falcon) formats, with each well containing one biopsy. The 96-well pipeline was then combined with the 1280 approved small molecules from the Prestwick chemical library. Plate and liquid handling were performed using a high-throughput screening platform system composed of a Sciclone G3 Liquid Handler from PerkinElmer (Waltham, MA, USA). At Day 0, tissues were treated either with the respective compound (1 mM stock solution) dissolved in 100% dimethyl sulfoxide (DMSO, Carl Roth) or DMSO alone. 0.5 μL of compounds in DMSO were transferred with a 96-array head to 200 μL DMEM/F12 medium per well to keep the final DMSO concentrations at 2.5 μM. Tissues were then incubated (37°C; 5% CO_2) for 72h prior to a second round of compound treatment, which was performed by exchanging cell culture medium per well and transferring 2.5 μM of compounds in DMSO into the fresh medium. After an incubation time of a further 48 h (37°C; 5% CO_2) the tissues were harvested and fixed for histological processing and imaging.

Splinted wound model

The splinted wound model was employed to simulate human skin healing due to the mouse skin containing the panniculus carnosus muscle, which is absent in human skin. The procedure is as follows: Following isoflurane anesthesia, depilation and disinfection of the dorsal region, a 6 mm diameter biopsy punch was used to inflict full-thickness wounds on either side of the dorsal spine. Immediately thereafter, a sterile silicone ring (inner diameter 8 mm) was positioned around the wound. This was secured to the surrounding skin using cyanoacrylate medical adhesive supplemented by four symmetrical 6-0 nylon sutures to inhibit wound contraction. Postoperative animal condition was monitored daily. Standardized wound photography was performed at 0, 7, 10, 14, and 21-days post-surgery. Wound area was analyzed using ImageJ to calculate healing rates. Tissue samples were collected from selected animals at each time point for histological assessment via hematoxylin and eosin (H&E) and Masson's trichrome staining.

Decellularized fascia preparation

After harvesting the fascia, decellularization was performed using repeated freeze-thaw cycles. The protocol consisted of freezing the tissue at −80°C for 30 min, followed by thawing at room temperature (approximately 20°C–25°C) for 30 min. This freeze-thaw cycle was repeated six times to achieve decellularization.

Migration & contraction measurements

Fascia tissues were recorded everyday by a brightfield microscope to check the invasion and contraction state of the tissues. The invasion index was calculated with the following formula: migration index= $(S_{Dn} - S_{D0})/S_{D0}$. S_{Dn} (n = 1, 2, 3, 4) and S_{D0} represent tissue size (including the migrated area) on Day 1, 2, 3, 4 and Day 0, respectively. The contraction index was calculated with the following formula: Contraction index= $(T_{D0} - T_{Dn})/T_{D0}$. T_{D4} (n = 1, 2, 3, 4) and T_{D0} represent original tissue size (excluding the migrated area) on Day 1, 2, 3, 4 and Day 0 respectively.

Histology

Except otherwise stated, all the samples were fixed overnight in 2% paraformaldehyde (VWR) in PBS at 4°C and washed three times with PBS. Samples were then embedded in optimal cutting temperature compound (OCT, Sakura Finetek) and snap frozen on dry ice. 6 μm frozen sections were made by a cryostat (Cryostar NX70, Thermo fisher) and frozen section slides were stored at −20°C. Masson's trichrome staining was applied using a trichrome stain kit (Sigma-Aldrich) according to the manufacturer's instructions. Images were recorded by a ZEISS AxioImager. Z2m (Carl Zeiss) with brightfield channel. In Masson's trichrome staining, muscle fibers and keratin are stained as red, collagen is stained as blue, cytoplasm is stained as light-red and cell nuclei is stained as black.

In vivo chemical treatment to unlock regeneration

All experiments were carried out on 7- to 8-week-old mice under isoflurane anesthesia (RWD Life Science). Wounds were inflicted using 6 mm full-thickness biopsy punches (Acuderm Inc), after which mice were housed in separate cages. One day after wounding, mice were injected subcutaneously with control or chemical solutions, with subsequent injections every 48-h afterward. Injection solution volume is 50 μL, consisting of 10% DMSO (Sigma), 40% PEG300 (Solarbio), 5% Tween-80 (Biosharp) and 45% saline (0.9% NaCl; Servicebio); treatment chemicals were dissolved in DMSO.

Whole mount tissue staining & imaging

For 3D whole mount imaging, fascia samples were immersed overnight in PBSGT (1x PBS implemented with 0.2% gelatin (Sigma), 0.5% Triton X-100 (Sigma) and 0.01% thimerosal (Sigma)) at room temperature and incubated with primary antibodies diluted in PBSGT for three days at room temperature. The tissues were then washed three times with PBSGT for at least 30 min each time and incubated with secondary antibodies diluted in PBSGT for one day. Finally, tissues were rinsed three times with PBSGT and stored in PBS at 4°C until imaging was conducted with a Leica SP8 multi-photon microscope. For all other imaging, tissue samples were fixed overnight in 2% paraformaldehyde (VWR) in PBS at 4°C and washed three times with PBS. Samples were then embedded in optimal cutting temperature compound (OCT, Sakura Finetek) and snap frozen on dry ice. 8 μm frozen sections were made by a cryostat (Cryostar NX70, Thermo fisher) and frozen section slides were stored at −20°C. Slides were incubated with 0.3% Triton X- for 30 min, washed three times with PBS containing 0.05% Tween 20 (Invitrogen, 003005) (PBST), then blocked with 5% Blocker BSA (Thermo Scientific, 37525) for 2 h at room temperature. Slides were then incubated with primary antibodies with 5% BSA overnight at 4°C. The next day, slides were washed three times with PBST, then incubated with secondary antibodies with 5% BSA for 2 h at room temperature in the dark. After that slides were washed three times with PBST, SlowFadeTM Gold with DAPI (Invitrogen, S36939) was added, and sealed with glass coverslips. Fluorescent imaging was conducted using a Leica DM6B or Leica Stellaris 8 confocal microscope. Primary antibodies used: αSMA (ab21027, ab124964, ab5694, Abcam), Caspase (ab32499, Abcam), Cytokeratin 14 (ab7800, Abcam), Corin (BS-7685R, Bioss), Ki67 (ab16667, ab21700, Abcam), Lef1 (#2230, Cell signaling), Pdpn (PDPN-112AP, Invitrogen; ab10288; Abcam), pStat3 (ab32143, Abcam), Rspo2 (PA5-25188, Invitrogen), Runx2 (20700-1-AP, Proreintech; ab92336, Abcam), Sox2 (11064-1-AP, Proteintech; PA1-094, Invitrogen), Yap (13584-1-AP, Proreintech). Secondary antibodies used: Donkey anti-rabbit AF647 (A-31573, Life Technologies), Donkey anti-goat AF647 (A-21447, Life Technologies), Goat anti-rabbit AF488 (ab150077, Abcam), Goat anti-rabbit AF594 (ab150080, Abcam).

Live imaging

Fascia tissue cultured in Matrigel was fixed in 2% low-melting agarose (Biozym) and left at room temperature to solidify. DMEM/F12 medium without phenol red was then added to keep the tissues alive during imaging. Four-dimension (4D) time-lapse images were performed by a Zeiss AxioObserver Z1 microscope for tissues obtained from *En1*^{cre};*R26*^{mCherry} mouse line or a Leica SP8 multi-photon microscope for tissues obtained from *En1*^{cre};*R26*^{mTmG} mouse line. Samples were placed in a qualified incubator with heating and gas control (Ibidi). The incubator temperature was adjusted to 35°C and was supported with 5% CO_2 during imaging. Brightfield and mCherry signals were recorded for tissues from *En1*^{cre};*R26*^{mCherry}; green fluorescent protein (GFP) and tdTomato signals were recorded for tissues from *En1*^{cre};*R26*^{mTmG}.

Single-cell tracking

4D time-lapsed imaging was subjected to maximum intensity projection in Imaris 9.3.1 (Bitplane) software. In addition to Full Track of individual cells during the entire length of a time-lapse, Dragon Tails enables visualization of previous or future steps (or both) for the track. Full track records the complete migration path of a cell, while the dragon tail reflects only the last few points of a path. The projected datasets were subjected to cell migration and cell-tracking analysis using the Trackmate function of ImageJ.[55] Datasets were binned at 15-min intervals to adequately capture the sprout-reticulate-cluster events. Variables, such as blob diameter, threshold and segmentation detector, were adjusted to suit the nature of the data and the samples. For the fourth dimension of the tracks, color ramp was applied to the individual tracks as a function of time (blue, first time point of the track; orange, last time point of the track).

ECM deposition and immunostaining assay

Human dermal fibroblast cell line FF95 was used for ECM deposition and immunostaining assay. Cells were seeded on glass-bottom plates coated with 1% Porcine Gelatin and cultured in complete medium with 5 ng/mL recombinant TGFβ1. Confluent cells were first incubated in double distilled water/0.1% Triton X-100 for 45 min, then in 2% sodium deoxycholate. Cells were then treated with 1 M NaCl and decellularized buffer (30 μg/mL DNase, 1.3mM $MgSO_4$, 2mM $CaCl_2$). The decellularized plate was then fixed with 4% PFA. After washing twice with PBS, plates were permeabilized with PBST (1% BSA $^{+}$0.1% Triton X- in PBS). Plates were next blocked with 1% BSA and 10% serum, according to the species of secondary antibody used during immunostaining. Lastly, plates were incubated overnight with primary antibody (collagen I, fibronectin), followed by 1 h incubation with secondary antibody and 10 min of DAPI. Finally, plates were imaged with a confocal microscope (LSM710, Zeiss).

QUANTIFICATION & STATISTICAL ANALYSIS

Data analysis

3D images and time series videos were processed with Imaris 9.3.1 (Bitplane). Brightness and contrast were modified to exclude false positive signals and to obtain better visibility. Fractal analysis was conducted using the ImageJ plug in 'FracLac'29 (FracLac 2015Sep090313a9390).[56] Fractal dimension (DF) values and Lacunarity (Lac) values were calculated using the box counting approach (slipping and tighten grids were set at default sample sizes, threshold of minimum pixel density was set as 0.40). Pairwise correlations were assessed in R using Pearson's correlation coefficient based on sample-level averages, and visualized using ggplot2. Fibroblast subpopulation calculations following chemical treatment were determined by dividing the number of fluorescent-positive cells by the number of DAPI-positive cells. All schematics were made using PowerPoint or Adobe Photoshop or BioRender.

Statistics & reproducibility

Statistical analysis was performed using GraphPad Prism software (Version 8.4, GraphPad). Statistical significance was determined using one-way ANOVA or students' *t* test, or as otherwise indicated in the corresponding figure legends. *p*-values reported "*" denotes $p > 0.05$, "**" denotes $p > 0.01$, and "***" denotes $p > 0.001$. Statistical details for individual experiments can be found in the main result text or in the figure legends. Unless otherwise stated, all results were repeated with at least three independent experiments or three biological samples ($n \geq 3$). All line and bar graph measurements show the mean values with standard deviation error bars. All cell tracking data were derived from individual movies. 3D staining was performed on two samples and images were recorded at three different sites of the samples.